

A General Safety Framework for Autonomous Manipulation in Human Environments

Jakob Thumm, Julian Balletshofer, Leonardo Maglanoc, Luis Muschal, and Matthias Althoff

Abstract—Autonomous robots are projected to significantly augment the manual workforce, especially in repetitive and hazardous tasks. For a successful deployment of such robots in human environments, it is crucial to guarantee human safety. State-of-the-art approaches to ensure human safety are either too conservative to permit a natural human-robot collaboration or make strong assumptions that do not hold for autonomous robots, e.g., knowledge of a pre-defined trajectory. Therefore, we propose the shield for Safe Autonomous human-robot collaboration through Reachability Analysis (SARA shield). This novel power and force limiting framework provides formal safety guarantees for manipulation in human environments while realizing fast robot speeds. As unconstrained contacts allow for significantly higher contact forces than constrained contacts (also known as clamping), we use reachability analysis to classify potential contacts by their type in a formally correct way. For each contact type, we formally verify that the kinetic energy of the robot is below pain and injury thresholds for the respective human body part in contact. Our experiments show that SARA shield satisfies the contact safety constraints while significantly improving the robot performance in comparison to state-of-the-art approaches.

Index Terms—Human-robot collaboration, safety, power and force limiting, manipulation, formal methods, constrained contacts, clamping, and autonomous robotics.

I. INTRODUCTION

Autonomous robots have already started to replace tedious, strenuous, and dangerous jobs [1, 2], and are projected to make up a relevant part of the future workforce [3, 4]. We require these autonomous robots to safely collaborate with humans while exerting a high level of interactivity. Previous approaches to ensure human safety in autonomous robotics often lack formal guarantees [5–10]. Most formal approaches, however, make assumptions that do not hold for fully autonomous robots, e.g., pre-defined trajectories that prevent human clamping [11, 12], no contacts with the robot links [11, 13], or stationary humans [11]. Formal approaches that do not make these assumptions [14] are often too conservative to enable a seamless human-robot collaboration (HRC).

ISO/FDIS 10218-2:2024 defines two possible forms of contact: *constrained contacts*, where the human is clamped by the robot link, and *unconstrained contacts*, where the human can freely move. Recent experiments have shown that the safe contact forces for unconstrained contacts are up to 20 times higher than for constrained contacts [15, 16]. Each contact comprises two phases: in the *transient* phase (first 0.5 s), peak

contact forces have to be limited to minimize the risk of injury; in the subsequent *quasi-static* phase, clamping forces have to remain below the pain onset thresholds. The quasi-static phase is negligible for unconstrained contacts.

To mitigate the downsides of previous work, we propose the shield for Safe Autonomous human-robot collaboration through Reachability Analysis (SARA shield). Our novel power and force limiting [17] approach formally guarantees human safety in robotic manipulation for (a) dynamically changing robot paths, (b) full human-robot contact, (c) arbitrary human motion, and (d) sharp robot geometries. Our framework focuses on limiting all transient contact forces and can be extended with any contact reaction scheme mitigating quasi-static forces, e.g., [18]. Figure 1 provides an overview of the methodology behind SARA shield. In each control cycle, SARA shield detects all possible contacts between the robot and the human by determining the sets of all possible states the human and robot can occupy in a given time frame using reachability analysis. Utilizing the same reachability analysis, we categorize the potential contacts into constrained and unconstrained types. Once a contact is detected and classified, we reduce the speed of the robot so that the kinetic energy of the robot link in contact is below the corresponding thresholds of the detected contact type. By differentiating the contacts by their type, we do not have to assume that all contacts are constrained and can verify against the less conservative unconstrained contacts in most situations. As we base SARA shield on the previous work on provably safe manipulation for reinforcement learning-based HRC [19], we can directly deploy SARA shield on autonomous robots.

Our core contributions are

- a formal safety framework for manipulators in human environments including,
- a reachability-based clamping detection, and
- an injury prevention based on admissible contact energies.

The main claims following our experimental results are that

- SARA shield significantly improves the robot performance in comparison to previous safe HRC approaches, and
- the kinetic energy of a robot controlled with SARA shield during a contact with a human is below injury thresholds.

This article is structured as follows: Sec. II discusses the related work. We introduce the notation of our reachability analysis, the foundation of our safety mechanism in Sec. III, and the problem statement in Sec. III-C. Sec. IV provides a high-level overview of our proposed safety framework. We discuss our proposed contact classification in Sec. V and our

¹The authors are with the School of Computation, Information and Technology, Technical University of Munich, 85748 Garching, Germany. {jakob.thumm, julian.balletshofer, althoff}@tum.de

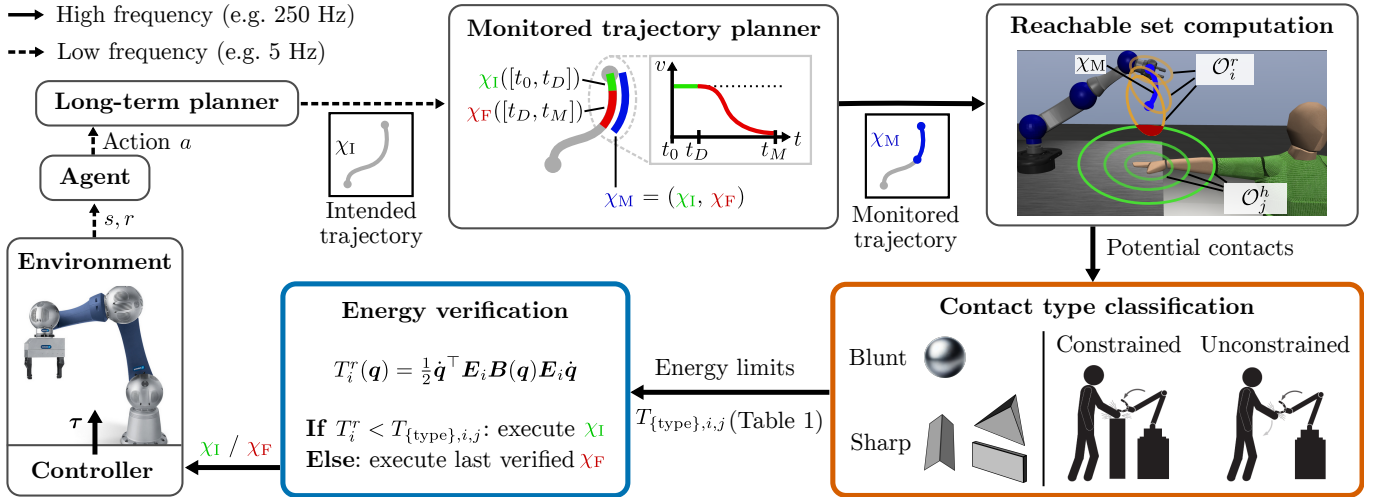


Fig. 1. Overview of the SaRA-shield safety framework. An action is translated into an intended trajectory. In each control cycle, SaRA shield computes a monitored trajectory consisting of an intended trajectory followed by a failsafe trajectory. We check the monitored trajectory for possible human contacts using reachability analysis. When a potential contact with the human is detected, we classify the contact into the constrained or unconstrained type. We verify if the kinetic energy of the robot upon contact is below pain and injury limits for the given contact type. If the verification is successful, we execute the intended trajectory, and if it fails, we execute the last successfully verified failsafe trajectory.

energy-based verification in Sec. VI. Finally, we evaluate our claims in Sec. VII and provide a conclusion in Sec. VIII.

II. RELATED WORK

This section introduces the notion of (a) speed and separation monitoring, (b) power and force limiting, and (c) discusses relevant methodologies implementing them. We subsequently discuss recent human injury and pain onset studies and their implications for safety in HRC.

A. Speed and Separation Monitoring

In speed and separation monitoring [17], the robot is stopped before a human can reach it. Industrial applications usually implement speed and separation monitoring by enclosing the workspace of the robot with a light curtain that stops the robot once it is crossed. The safety distance between the robot and the human can be decreased when a variable braking time of the robot and a limited human speed is assumed [20, 21]. When the human position can be continuously measured, the robot can resume its operation once the human retreats far enough from its workspace. The authors in [12, 19, 22–24] propose a formal speed and separation monitoring concept by over-approximating the reachable sets of the robot and surrounding humans. These approaches allow the robot to continue operation even if the human is relatively close (≈ 0.2 m), assuming continuous measurements of the human pose are available.

B. Power and Force Limiting

In many HRC scenarios, we want to allow or even embrace contact with the human partner. ISO/FDIS 10218-2:2024 permits such contacts using power and force limiting, where the robot is allowed to have a non-zero speed at contact as long as transient and quasi-static force, pressure, or energy limits are

not violated. It is important to note that not every body part can endure the same contact forces, as we discuss in Sec. II-C. Therefore, methods that do not assume knowledge about the human pose have to assume the worst case and tend to be conservative in their maximal allowed robot speed.

First approaches implementing power and force limiting proposed to stop the robot once a contact is detected based on an external force estimation from motor current differences [5, 6, 18]. However, as shown in [15, 25], the reaction time of such approaches is too slow to significantly mitigate the initial transient contact force spikes. Hence, these methods are mostly relevant for reducing contact forces in the quasi-static phase.

ISO/FDIS 10218-2:2024 defines a basic power and force limiting method that approximates the robot mass acting on the contact as half of the total robot mass and calculates the maximal contact forces based on the kinetic energy of the robot. Although it is an easy-to-use model, Kirschner et al. [26] have shown that this robot mass calculation is incorrect, and the reflected robot mass [27] should be used instead. ISO/FDIS 10218-2:2024 also specifies a reduced-speed mode, where any contact is considered safe while the robot speed is below 0.25 m s^{-1} . However, this approach violates contact force thresholds for large robot masses [15] and only permits blunt robot geometries. Hence, we argue that the simple safety measures outlined in ISO/FDIS 10218-2:2024 do not provide formal safety guarantees for all collaborative robots.

Haddadin et al. [11] propose a power and force limiting approach based on the reflected robot mass, where they assume (a) knowledge of the human pose, (b) that the human is stationary, and (c) the critical contact point is known. Using these assumptions, they determine the contact normal between the robot and the human, along which they calculate the reflected robot mass. Haddadin et al. [11] are also the first to propose the direct use of an injury database to determine a so-called safe motion unit, which returns the maximal allowed

speed of the robot given the reflected robot mass. They argue that this leads to a more accurate representation of the injury cases than the usually used transient force limits. Finally, they scale the speed of the robot to the maximal allowed value in each control cycle. The major downside of this approach is the assumed knowledge of the contact normal, which does not hold in reality.

To overcome this limitation, Steinecker et al. [10] propose to use the mean reflected mass over all possible contact normals as a mass metric. However, this approximation cannot provide formal safety guarantees. Instead of verifying human safety based on the reflected mass, recent works [14, 28] propose to use an energy tank-based control to limit the total kinetic energy of the robot. However, these approaches do not take the human pose and contact type into account and thus have conservative energy thresholds.

A downside of most power and force limiting approaches [5, 6, 10, 11, 14, 29–33] is the assumption that a contact is always possible, leading to a reduced speed of the robot even if the human is far away. To overcome this, the authors in [7, 8] propose to switch between power and force limiting and speed and separation monitoring based on the distance between the human and the robot. The approach in [12] extends this idea by dynamically reducing the speed of the robot if a possible contact is detected using reachability analysis. Liu and Althoff [13] further improve on this by replacing the otherwise fixed maximal contact speed with a dynamic one that is verified using model conformance checking. Despite promising results, their approach is only applicable to end-effector contacts and requires human contact measurements for each new robot, body part, and a wide range of participants.

C. Human Injuries

Human pain onset and skin damage depend on the impact energy, contact type, and contact shape [11, 34–37]. The most researched contact situations are constrained contacts with blunt impactors that evaluate the subjective onset of pain [36–39]. ISO/FDIS 10218-2:2024 defines force, pressure, and energy limits for constrained contacts, which seem to be confirmed by the aforementioned experimental studies. However, there remains a large variance in the study outcomes. When it comes to sharp or edged contacts in constrained contacts, the ex-vitro study of Kirschner et al. [40] shows that the ISO-defined limits are too high to prevent skin damage. A subsequent study for unconstrained contacts [16] showed that critical skin injuries occur at 5–20 times higher impact velocities than in the constrained case. These studies show that sharp contact geometries should be taken into account and that if no contact classification is performed, safety mechanisms have to assume the more conservative constrained contact type at all times.

III. PRELIMINARIES AND PROBLEM STATEMENT

This section introduces reachability analysis, the safety shield concept we are building upon, our problem statement, and the assumptions we make.

A. Reachability Analysis

We adopt a reachability analysis approach for safety verification. Our considered systems follow the dynamics $\dot{\mathbf{x}}(t) = f(\mathbf{x}(t), \mathbf{u}(t), \mathbf{w}(t))$, with time $t \in \mathbb{R}_0^+$, state $\mathbf{x}(t) \in \mathbb{R}^n$, input $\mathbf{u}(t) \in \mathcal{U} \subset \mathbb{R}^m$, and disturbance $\mathbf{w}(t) \in \mathcal{W} \subset \mathbb{R}^p$, where \mathcal{U} and \mathcal{W} are compact sets. For the given initial state \mathbf{x}_0 , input trajectory $\mathbf{u}(\cdot)$ ¹, and disturbance trajectory $\mathbf{w}(\cdot)$, we denote the unique solution of the system dynamics as $\chi(t; \mathbf{x}_0, \mathbf{u}(\cdot), \mathbf{w}(\cdot)) \in \mathbb{R}^n$. The exact reachable set of the system at time t can be defined for a set of initial states \mathcal{X}_0 as

$$\mathcal{X}^e(t) = \{ \chi(t; \mathbf{x}_0, \mathbf{u}(\cdot), \mathbf{w}(\cdot)) \mid \mathbf{x}_0 \in \mathcal{X}_0, \forall \tau \in [t_0, t] : \mathbf{u}(\tau) \in \mathcal{U}, \mathbf{w}(\tau) \in \mathcal{W} \}. \quad (1)$$

In general, the exact reachable set $\mathcal{X}^e(t)$ cannot be computed [41], so we compute over-approximations for particular points in time $\mathcal{X}(t) \supseteq \mathcal{X}^e(t)$, which we simply refer to as the reachable set for simplicity. All states reachable during the time interval $[t_a, t_b]$ are denoted by $\mathcal{X}([t_a, t_b]) = \bigcup_{t \in [t_a, t_b]} \mathcal{X}(t)$.

Let us introduce the operator $\text{occ}()$ returning the possible occupancies of a system for a given reachable set. We denote the set of points that a system can occupy in Euclidean space at time t and the time interval $[t_a, t_b]$ as $\mathcal{O}(t) = \text{occ}(\mathcal{X}(t))$ and $\mathcal{O}([t_a, t_b]) = \text{occ}(\mathcal{X}([t_a, t_b]))$, respectively, and further refer to them as reachable occupancies. Similarly, we define the reachable velocity as the set of linear velocities that any point of the system can have in the time interval $[t_a, t_b]$ as $\mathcal{V}([t_a, t_b]) = \text{vel}(\mathcal{X}([t_a, t_b]))$, where $\text{vel} : \mathcal{P}(\mathbb{R}^n) \rightarrow \mathcal{P}(\mathbb{R}^3)$ extracts all possible linear velocities from a reachable set and \mathcal{P} is the power set. We denote the set of all human body parts in the scene as $\mathcal{H} = \{h_1, \dots, h_M\}$ and the set of robot links as $\mathcal{R} = \{r_1, \dots, r_N\}$. A point in Euclidean space is denoted as \mathbf{p} , and a capsule is defined by two points $\mathbf{p}_1 \in \mathbb{R}^3$ and $\mathbf{p}_2 \in \mathbb{R}^3$ and a radius $r \in \mathbb{R}^+$ with $\mathcal{C}(\mathbf{p}_1, \mathbf{p}_2, r) = \overline{\mathbf{p}_1 \mathbf{p}_2} \oplus \mathcal{B}(\mathbf{0}, r)$, where $\overline{\mathbf{p}_1 \mathbf{p}_2}$ is the line segment between \mathbf{p}_1 and \mathbf{p}_2 , $\mathcal{B}(c, r)$ is a ball with center c and radius r , the symbol \oplus represents the Minkowski sum, and $\mathbf{0}$ is the vector of zeros. A polytope is defined in the halfspace representation as $\mathbb{H}(N, \mathbf{d}) = \{ \mathbf{p} \in \mathbb{R}^3 \mid N\mathbf{p} \leq \mathbf{d}, N \in \mathbb{R}^{H \times 3}, \mathbf{d} \in \mathbb{R}^H \}$ [42, Sec. 2.5]. The operations $N[h]$ and $\mathbf{d}[h]$ index the h -th row vector of the matrix N and the h -th entry of the vector \mathbf{d} , respectively. Finally, we define the signed distance function between a point \mathbf{p} and a set \mathcal{S} as

$$\text{sd}(\mathbf{p}, \mathcal{S}) = \begin{cases} - \inf_{\mathbf{p}_s \in \partial \mathcal{S}} \|\mathbf{p} - \mathbf{p}_s\|_2, & \mathbf{p} \in \mathcal{S} \\ \inf_{\mathbf{p}_s \in \partial \mathcal{S}} \|\mathbf{p} - \mathbf{p}_s\|_2, & \mathbf{p} \notin \mathcal{S}. \end{cases} \quad (2)$$

B. Safety Shield

To ensure the safety of robots controlled by autonomous agents, we adapt the safety shield for manipulators proposed in [19]. The safety shield relies on the existence of a set of invariably safe states that can be reached from any state. Thumm and Althoff [19] define the set of invariably safe states

¹Note that $\mathbf{u}(\cdot)$ refers to the input trajectory and $\mathbf{u}(t)$ refers to the input at time t .

as a fully stopped robot for manipulators in accordance with the speed and separation monitoring formulation in ISO/FDIS 10218-2:2024. Thumm and Althoff [19] further demonstrate that a safety shield for autonomous agents is less conservative when it operates on a higher frequency than the output frequency of the agent. Therefore, they convert each action of the agent \mathbf{a} into a set of goal states $\mathcal{X}_g(\mathbf{a})$, and aim to steer the robot towards this set for L time steps, while performing a safety shield update at every time step.

In each safety shield update, Thumm and Althoff [19] compute an intended and a failsafe trajectory. Without loss of generality, we always reset the clock to $t_0 = 0$ at each time step. The intended trajectory χ_I steers the robot towards $\mathcal{X}_g(\mathbf{a})$ using the output $\mathbf{u}_{\Phi_I}(\mathbf{x}, \mathcal{X}_g(\mathbf{a}))$ of the intended controller for D time steps; in this work, we use $D = 1$. The failsafe trajectory χ_F steers the robot to an invariably safe state using the output $\mathbf{u}_{\Phi_F}(\mathbf{x}, \mathcal{X}_g(\mathbf{a}))$ of the failsafe controller for k_F time steps ending at time t_M . Their failsafe controller performs a braking maneuver that is path-consistent with the intended trajectory, which prevents the robot from deviating from the set of goal states. The shield appends a full failsafe trajectory to an intended trajectory to form a so-called monitored trajectory

$$\chi_M = \begin{cases} \chi_I(t; \mathbf{x}_0, \mathbf{u}_{\Phi_I}(\cdot), \mathbf{w}(\cdot)), & t \in [t_0, t_D] \\ \chi_F(t; \mathbf{x}_D, \mathbf{u}_{\Phi_F}(\cdot), \mathbf{w}(\cdot)), & t \in [t_D, t_M]. \end{cases} \quad (3)$$

If the safety of the monitored trajectory is verified successfully, the robot executes the intended trajectory, and otherwise the failsafe trajectory from the last successfully verified monitored trajectory. When assuming that the robot starts from an invariably safe state, safety is ensured indefinitely by induction [23, p. 5].

The authors in [12, 19] verify the monitored trajectory against the specification that a contact between the human and robot should be prevented entirely. For this, they compute the reachable occupancies of all human body parts $h_j \in \mathcal{H}$ in the time interval $[t_0, t_M]$ denoted as $\mathcal{O}_j^h([t_0, t_M])$ assuming that the human inputs stem from a compact set $\mathbf{u}_j^h(t) \in \mathcal{U}_j^h$, e.g., each human body part can have a maximal speed of 1.6 m s^{-1} as defined in [43]. They further compute the reachable occupancies of all robot links $r_i \in \mathcal{R}$ following the monitored trajectory as $\mathcal{O}_i^r([t_0, t_M])$.

The verification evaluates the safety of the monitored trajectory for all time intervals, robot links, and human body parts, defining the constraint

$$c_{\text{safe}}(\chi_M) := \bigwedge_{a=0}^{M-1} \bigwedge_{r_i \in \mathcal{R}} \bigwedge_{h_j \in \mathcal{H}} c_{\text{safe}, i, j}([t_a, t_{a+1}]). \quad (4)$$

Thumm and Althoff [19] consider the movement of a robot link r_i to be safe in the time interval $[t_a, t_b]$ with respect to the body part h_j if their reachable occupancies do not intersect

$$c_{\text{safe}, i, j}([t_a, t_b]) = \bar{c}_{\text{contact}, i, j}([t_a, t_b]), \\ \bar{c}_{\text{contact}, i, j}([t_a, t_b]) := \mathcal{O}_j^h([t_a, t_b]) \cap \mathcal{O}_i^r([t_a, t_b]) = \emptyset, \quad (5)$$

where \bar{c} is the negation of the predicate c . Schepp et al. [24] enables an efficient computation of these reachable occupancies and intersection checks, using capsules as reachable occupancies of the robot links and human body parts.

C. Problem Statement

We aim to derive a safety framework that allows the robot to come into contact with the human as long as it is slow enough to prevent injuries. For this, we want to operate the robot at high speed as long as possible and only reduce the speed if necessary. ISO/FDIS 10218-2:2024 provides three types of contact constraints: force, pressure, and energy, from which we are using the energy constraints for our problem statement. We aim to minimize a general objective J_g while ensuring that if a contact with the human is possible, the robot energy is below human pain and injury limits with

$$\min_{\mathbf{u}_{\Phi}} J_g \quad (6a)$$

$$\text{subject to } \chi(t_g; \mathbf{x}_0, \mathbf{u}_{\Phi}(\cdot), \mathbf{w}(\cdot)) \in \mathcal{X}_g(\mathbf{a}), \quad (6b)$$

$$\forall r_i \in \mathcal{R}, h_j \in \mathcal{H}, t \in [t_0, t_g]: \quad (6c)$$

$$\mathcal{O}_j^h(t) \cap \mathcal{O}_i^r(t) = \emptyset \vee T_i^r(t) \leq T_{i,j}, \quad (6d)$$

$$\mathbf{u}_j^h(\cdot) \in \mathcal{U}_j^h, \mathbf{u}_{\Phi}(\cdot) \in \mathcal{U}, \mathbf{w}(\cdot) \in \mathcal{W}, \quad (6e)$$

where t_g is the time the robot needs to reach the set of goal states, $T_i^r(t)$ describes the maximal reachable kinetic energy that robot link r_i induces into the human contact at time t , and $T_{i,j}$ denotes the energy threshold at which a rigid body with the geometry of robot link r_i is unlikely to cause an injury for the human body part h_j . In our experiments, we always set the objective to minimizing the time to reach the goal $J_g = t_g$. However, other objectives such as additionally minimizing the jerk or motor currents would be possible. Note that the contact energy constraint can be converted into force or pressure constraints if we assume knowledge about the stiffness and damping properties of the human skin as detailed in Annex M of ISO/FDIS 10218-2:2024.

D. Assumptions

Similar to Thumm and Althoff [19], we make three key assumptions in this work. First, we assume that the human pose is measurable with a bounded measurement error of δ_{meas} and a bounded time delay of Δt_{meas} . In our experiments, we achieve this by using a motion-tracking system, but our formulation can also be used with laser scanners [44] or depth cameras [45–48]. The measurement error and delay are incorporated into the human reachable set computation using the set-based prediction in [24]. Second, we assume that the speed of any human body part never exceeds 1.6 m s^{-1} when approaching the robot, as defined in DIN EN ISO 13855:2010.

Third, we assume that the intended and failsafe controller track the desired trajectory with a bounded tracking error, which is incorporated in the bounded system noise \mathcal{W} of the robot reachable occupancy computation \mathcal{O}^r [24]. In our experiments, we are using a PD-controller for trajectory tracking, but prior work has effectively demonstrated bounded tracking error guarantees for a trajectory tracking controller based on model conformance checking [49]. Given the controller, for all joints $i = 1, \dots, N$, we assume knowledge of the maximal

possible joint velocities \hat{q}_i , acceleration $\hat{\ddot{q}}_i$, and jerk $\hat{\dddot{q}}_i$ over all trajectories and for all times t with

$$\hat{q}_i = \sup_{t \leq \tau \leq t + \Delta t} |\dot{q}_i(\tau)| \quad (7)$$

$$\hat{\ddot{q}}_i = \sup_{t \leq \tau \leq t + \Delta t} |\ddot{q}_i(\tau)| \quad (8)$$

$$\hat{\dddot{q}}_i = \sup_{t \leq \tau \leq t + \Delta t} |\dddot{q}_i(\tau)|, \quad (9)$$

where $\Delta t = t_1 - t_0$.

We additionally assume that through knowledge of the robot kinematics, we can determine the linear and angular velocity and acceleration of a point on the robot at a given time with bounded errors of $\|\mathbf{w}_v\|_2 = \|\dot{\mathbf{p}} - \dot{\mathbf{p}}^e\|_2 \leq w_{v,\max}$, $\|\mathbf{w}_\omega\|_2 = \|\boldsymbol{\omega} - \boldsymbol{\omega}^e\|_2 \leq w_{\omega,\max}$, $\|\mathbf{w}_a\|_2 = \|\ddot{\mathbf{p}} - \ddot{\mathbf{p}}^e\|_2 \leq w_{a,\max}$, and $\|\mathbf{w}_{\dot{\omega}}\|_2 = \|\dot{\boldsymbol{\omega}} - \dot{\boldsymbol{\omega}}^e\|_2 \leq w_{\dot{\omega},\max}$, respectively, where $(\cdot)^e$ indicates the true value. We can, e.g., use reachset conformance checking [50] to establish these error bounds.

Similarly to most power and force limiting approaches [7, 8, 10–14, 29, 31–33], we also assume that the human does not actively move into hurtful contact with the robot so that the speed difference between the human and the robot along the contact normal is always smaller or equal to the robot speed.

For classifying contacts, we additionally assume there is an over-approximating time-independent polytope representation of all environment elements that can cause clamping. This information is typically available in industrial applications or can be obtained using laser scanning [51].

IV. SAFETY FRAMEWORK FOR HUMAN-ROBOT INTERACTION

As highlighted in Sec. II-C, unconstrained contacts permit a significantly higher transient contact force than constrained contacts [16, 40]. Therefore, we propose for the first time to classify possible contacts into constrained and unconstrained types using reachability analysis. We then constrain the kinetic energy of the robot links at the contact points to be below the pain and injury limits for the respective contact type.

For the verification in (4), we define the safety constraint for a given robot link r_i , human body part h_j , and time interval $[t_a, t_b]$ as

$$c_{\text{safe},i,j}([t_a, t_b]) := \bar{c}_{\text{contact},i,j}([t_a, t_b]) \vee (c_{\text{free},i,j}([t_a, t_b]) \wedge c_{T,\text{free},i,j}) \vee (\bar{c}_{\text{free},i,j}([t_a, t_b]) \wedge c_{T,\text{clamp},i,j}), \quad (10)$$

where

- $\bar{c}_{\text{contact},i,j}$ evaluates if there is no contact between the robot link r_i and the human body part h_j ,
- $c_{\text{free},i,j}$ evaluates if the contact between link r_i and human body part h_j is an unconstrained contact,
- $c_{T,\text{free},i,j}$ evaluates if the kinetic energy of link r_i is below the injury threshold of body part h_j for unconstrained contacts, and
- $c_{T,\text{clamp},i,j}$ evaluates if the kinetic energy of link r_i is below the pain and injury threshold of body part h_j for constrained contacts.

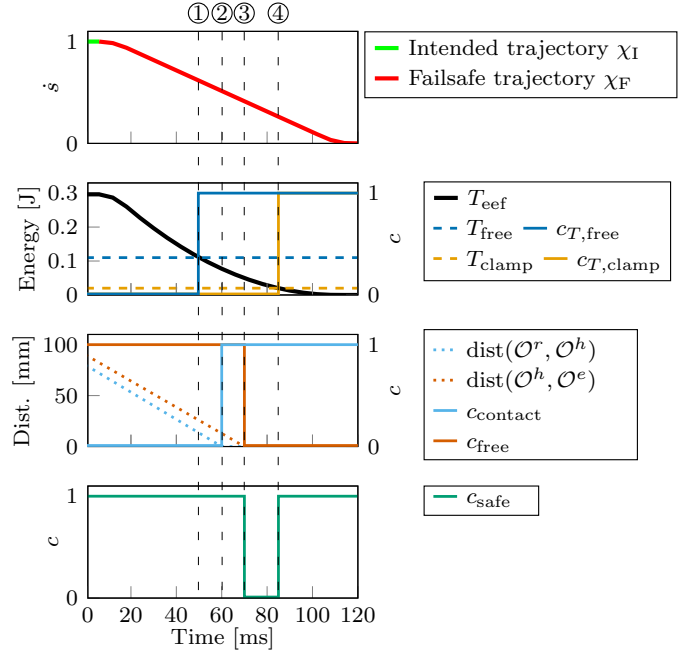


Fig. 2. Example evolution of the constraints in (10) over a monitored trajectory. ① The kinetic energy of the robot end effector T_{eeef} drops below the threshold for unconstrained contacts T_{free} , so $c_{T,\text{free}} = \text{true}$. ② The reachable occupancies of the robot and the human intersect ($\text{dist}(\mathcal{O}^r, \mathcal{O}^h) \leq 0$), indicating that an unconstrained contact is possible, but the robot energy is safe. ③ The human occupancy intersects with the environment ($\text{dist}(\mathcal{O}^h, \mathcal{O}^e) \leq 0$) and the robot ($\text{dist}(\mathcal{O}^r, \mathcal{O}^h) \leq 0$), indicating that a constrained contact is possible. Since the robot energy is violating the constrained contact energy threshold $T_{\text{eeef}} \geq T_{\text{clamp}}$, the trajectory is unsafe $c_{\text{safe}} = \text{false}$. ④ The robot energy drops below the constrained contact threshold, but once one time interval of the trajectory is unsafe, the entire trajectory is unsafe.

A typical evolution of these constraints over the length of a monitored trajectory is depicted in Fig. 2. We derive $c_{\text{free},i,j}$ in Sec. V and $c_{T,\{\text{type}\},i,j}$ in Sec. VI.

V. CONSTRAINED CONTACT DETECTION

In this section, we present how we can use reachability analysis to detect potential constrained contacts. In general, the human can be clamped between the robot and the static environment or in between two robot links. We will refer to these two cases as environmentally constrained contacts (ECCs) and self-constrained contacts (SCCs). Hence, we can ensure that a contact between link r_i and body part h_j in the time interval $[t_a, t_b]$ is unconstrained if

$$c_{\text{free},i,j}([t_a, t_b]) := \bar{c}_{\text{ECC},i,j}([t_a, t_b]) \wedge \bar{c}_{\text{SCC},i,j}([t_a, t_b]), \quad (11)$$

i.e., the contact is neither an ECC ($\bar{c}_{\text{ECC},i,j}$) nor an SCC ($\bar{c}_{\text{SCC},i,j}$). In the following subsections, we derive the general constraints $\bar{c}_{\text{ECC},i,j}$ and $\bar{c}_{\text{SCC},i,j}$, formulate a series of relaxations of those constraints, and discuss how we handle clamping of multiple human body parts. Figure 3 visualizes these concepts for the example of an ECC.

A. General ECC and SCC Constraints

We model the environment as a set of large unmovable elements $\mathcal{E} = \{e_1, \dots, e_K\}$, such as walls, the floor, or a table,

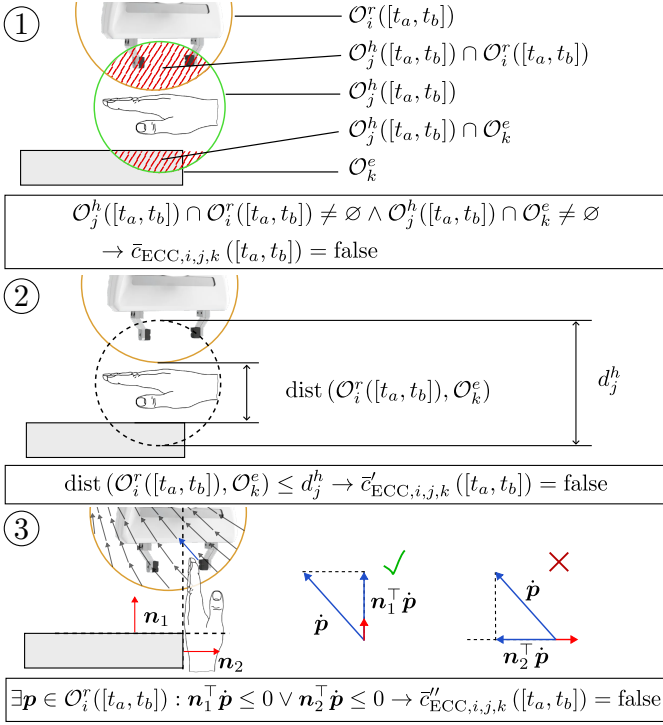


Fig. 3. Example of clamping constraints: ① Since the reachable occupancy of the human intersects the ones of the robot and environment element, clamping is possible. ② The smallest distance of the robot to the environment element is smaller than the human diameter, so clamping is possible. ③ There exists a point in the reachable occupancy of the robot that is moving towards the vertical face of the environment element, which could cause clamping as illustrated.

with fixed occupancies $\mathcal{O}_k^e, e_k \in \mathcal{E}$. We define a trajectory χ_M to be free of ECCs between a robot link r_i and a human body part h_j in a time interval $[t_a, t_b]$ if:

$$\bar{c}_{\text{ECC},i,j}([t_a, t_b]) := \bigwedge_{e_k \in \mathcal{E}} \bar{c}_{\text{ECC},i,j,k}([t_a, t_b]) \quad (12)$$

$$\bar{c}_{\text{ECC},i,j,k}([t_a, t_b]) := \mathcal{O}_j^h([t_a, t_b]) \cap \mathcal{O}_k^e = \emptyset, \quad (13)$$

i.e., there cannot be an ECC with the environment element e_k if the reachable occupancy of the human body part does not intersect with it.

For SCCs, we exclude a potential clamping of a body part h_j between two robot links $r_i, r_l \in \mathcal{R}, r_i \neq r_l$ in a time interval $[t_a, t_b]$ if:

$$\bar{c}_{\text{SCC},i,j,l}([t_a, t_b]) := \bar{c}_{\text{contact},i,j}([t_a, t_b]) \vee \bar{c}_{\text{contact},l,j}([t_a, t_b]), \quad (14)$$

i.e., there is no SCC if the human occupancy does not intersect with two different robot links. Based on (14), we define the SCC constraint for a link r_i and a body part h_j as

$$\bar{c}_{\text{SCC},i,j}([t_a, t_b]) := \bigwedge_{r_l \in \mathcal{R} \setminus r_i} \bar{c}_{\text{SCC},i,j,l}([t_a, t_b]). \quad (15)$$

B. Reducing Conservatism

The constraints in (12) and (15) are quite conservative and would be often violated in close HRC. Therefore, we subsequently propose three adaptations that reduce the conservatism of these constraints.

1) *Human Diameter*: A natural condition that is required for constrained contacts is that the shortest distance between the robot link r_i and environment element e_k (ECC) or the two robot links r_i and r_l (SCC) must be smaller or equal to the maximal diameter of the human body part that could be clamped. Therefore, we extend the constraints in (13) to

$$\bar{c}'_{\text{ECC},i,j,k}([t_a, t_b]) := \bar{c}_{\text{ECC},i,j,k}([t_a, t_b]) \vee \text{dist}(\mathcal{O}_i^r([t_a, t_b]), \mathcal{O}_k^e) > d_j^h, \quad (16)$$

and the one in (14) to

$$\bar{c}'_{\text{SCC},i,j,l}([t_a, t_b]) := \bar{c}_{\text{SCC},i,j,l}([t_a, t_b]) \vee \text{dist}(\mathcal{O}_i^r([t_a, t_b]), \mathcal{O}_l^r([t_a, t_b])) > d_j^h, \quad (17)$$

where dist is a distance function that measures the smallest distance between two sets and d_j^h is the diameter of the human body part. In Euclidean space, the distance function can be described as

$$\text{dist}(\mathcal{S}_1, \mathcal{S}_2) = \inf_{\mathbf{p}_1, \mathbf{p}_2} \|\mathbf{p}_1 - \mathbf{p}_2\|_2, \mathbf{p}_1 \in \mathcal{S}_1, \mathbf{p}_2 \in \mathcal{S}_2, \quad (18)$$

which we can efficiently compute for capsule representations [52, Ch. 10]. DIN 33402-2:2020-12 defines the 5, 50, and 95 percentile of human body part dimensions. Hence, we use the 95 percentile measurements as an upper bound for the diameters of human body parts and assume that the system is informed if a user with a particularly large body size operates next to the robot.

2) *Robot Velocity*: Clamping of a human body part between a point on the robot and a rigid body is only possible if the robot point lies outside of the rigid body and is moving towards it, i.e., the signed distance between the point and the rigid body is positive and increasing. Therefore, we can exclude clamping for a robot link r_i and a rigid body b_n with occupancy \mathcal{O}_n^b in the time interval $[t_a, t_b]$ if

$$\forall t \in [t_a, t_b] : \forall \mathbf{p} \in \mathcal{O}_i^r(t) : \mathbf{p} \notin \mathcal{O}_n^b(t) \wedge \frac{d}{dt} \text{sd}(\mathbf{p}, \mathcal{O}_n^b(t)) \geq 0, \quad (19)$$

i.e., the signed distance of any point in $\mathcal{O}_i^r(t)$ to $\mathcal{O}_n^b(t)$ is increasing if that point lies outside of $\mathcal{O}_n^b(t)$.

In our case, the rigid body can be another robot link (SCC) or an environment element (ECC), so $b_n \in (\mathcal{R} \setminus r_i) \cup \mathcal{E}$. In the case of SCCs, we express the velocity of robot link r_i in the frame of the other robot link r_l , and over-approximate the reachable occupancy of robot link r_l with a polytope. As such, we treat the robot link r_l as a static polytope and derive the formal verification for an arbitrary rigid body b_n .

To verify (19), it is insufficient to check if the smallest distance between the two sets is increasing, i.e., $\text{dist}(\mathcal{O}_i^r(t_b), \mathcal{O}_n^b(t_b)) > \text{dist}(\mathcal{O}_i^r(t_a), \mathcal{O}_n^b(t_a))$, as any point on the robot can cause clamping, not just the closest point to the rigid body. See part ③ of Fig. 3 as an example, where the closest point is moving away from the environment element, but clamping is still possible. Instead, we propose to verify (19) for constrained contacts involving rigid bodies which occupancy is enclosed by one or several polytopes.

Proposition V.1. A constrained contact involving the robot link r_i and a rigid body b_n with enclosing polytope $\mathbb{H}(\mathbf{N}, \mathbf{d})$, $\mathbf{N} \in \mathbb{R}^{H \times 3}$ in the time interval $[t_a, t_b]$ can be excluded if

$$\begin{aligned} \mathcal{O}_i^r([t_a, t_b]) \cap \mathbb{H}(\mathbf{N}, \mathbf{d}) &= \emptyset \wedge \\ \forall \mathbf{n} \in \mathcal{N}_{i,n} : \forall \dot{\mathbf{p}} \in \mathcal{V}_i^r([t_a, t_b]) : \mathbf{n}^\top \dot{\mathbf{p}} &\geq 0, \end{aligned} \quad (20)$$

where $\mathcal{N}_{i,n}$ is the set of normal vectors defining the clamping-relevant halfspaces of the enclosing polytope with

$$\begin{aligned} \mathcal{N}_{i,n} &= \{\mathbf{N}[h]^\top \mid h = 1, \dots, H : \exists \mathbf{p} \in \mathcal{O}_i^r([t_a, t_b]) : \\ &\mathbf{N}[h]\mathbf{p} > \mathbf{d}[h]\}. \end{aligned} \quad (21)$$

Proof. We prove (20) \implies (19) by contraposition, i.e.,

$$\begin{aligned} \exists t \in [t_a, t_b] : \exists \mathbf{p} \in \mathcal{O}_i^r(t) : \mathbf{p} \in \mathbb{H} \vee \frac{d}{dt} \text{sd}(\mathbf{p}, \mathbb{H}) < 0 & \quad (22) \\ \implies \mathcal{O}_i^r([t_a, t_b]) \cap \mathbb{H}(\mathbf{N}, \mathbf{d}) \neq \emptyset \vee \exists h = 1, \dots, H : \\ (\exists \mathbf{p} \in \mathcal{O}_i^r([t_a, t_b]) : \mathbf{N}[h]\mathbf{p} > \mathbf{d}[h]) \wedge \\ (\exists \dot{\mathbf{p}} \in \mathcal{V}_i^r([t_a, t_b]) : \mathbf{N}[h]\dot{\mathbf{p}} < 0). \end{aligned}$$

For the case that $\exists t \in [t_a, t_b] : \exists \mathbf{p} \in \mathcal{O}_i^r(t) : \mathbf{p} \in \mathbb{H}$, we get by definition of the reachable occupancy that $\exists t \in [t_a, t_b] : \exists \mathbf{p} \in \mathcal{O}_i^r(t) : \mathbf{p} \in \mathbb{H} \implies \mathcal{O}_i^r([t_a, t_b]) \cap \mathbb{H}(\mathbf{N}, \mathbf{d}) \neq \emptyset$. For the opposite case, let \mathbf{n}_p be the normal vector defining the supporting hyperplane of a point $\mathbf{p} \notin \mathbb{H}$ on \mathbb{H} , and let $\mathcal{H}_p = \{h \mid h = 1, \dots, H, \mathbf{N}[h]\mathbf{p} > \mathbf{d}[h]\}$ be the set of active polytope constraints for the point \mathbf{p} . Then, we can write $\mathbf{n}_p = \sum_{h \in \mathcal{H}_p} \lambda_h \mathbf{N}[h]^\top$ with $\lambda_h \geq 0$ [53, Sec. 8.1.2]. Let the halfspace defined by the hyperplane with normal vector \mathbf{n}_p be $\mathcal{S}(\mathbf{n}_p, d_p) = \{\mathbf{p}_p \mid \mathbf{n}_p^\top \mathbf{p}_p \leq d_p\}$. The signed distance function for a halfspace is $\text{sd}(\mathbf{p}, \mathcal{S}(\mathbf{n}_p, d_p)) = \mathbf{n}_p^\top \mathbf{p} - d_p$ with $\frac{d}{dt} \text{sd}(\mathbf{p}, \mathcal{S}(\mathbf{n}_p, d_p)) = \mathbf{n}_p^\top \dot{\mathbf{p}}$ if we assume a static polytope. By definition of the supporting hyperplane $\text{sd}(\mathbf{p}, \mathbb{H}) = \text{sd}(\mathbf{p}, \mathcal{S}(\mathbf{n}_p, d_p))$. Therefore, $\frac{d}{dt} \text{sd}(\mathbf{p}, \mathbb{H}) < 0 \implies \sum_{h \in \mathcal{H}_p} \lambda_h \mathbf{N}[h]\dot{\mathbf{p}} < 0 \implies \exists h \in \mathcal{H}_p : \mathbf{N}[h]\dot{\mathbf{p}} < 0$, which proofs Proposition V.1 as all possible robot velocities are contained in $\mathcal{V}_i^r([t_a, t_b])$. \square

In the following paragraph, we present how we efficiently evaluate (20) in practice.

a) *Computation of the Reachable Velocity:* In SARA shield, we use capsules to represent the reachable occupancies of the robot links as described in Sec. III-B. We denote the linear and angular velocity of a point \mathbf{p} as $\mathbf{v} = [\dot{\mathbf{p}}, \boldsymbol{\omega}]^\top$.

Proposition V.2. All points in a capsule $\mathcal{C}(\mathbf{p}_1, \mathbf{p}_2, r)$ with $\mathbf{v}_1 = [\dot{\mathbf{p}}_1, \boldsymbol{\omega}]^\top$ are moving away from a plane with normal vector \mathbf{n} if

$$\check{v}_n = \mathbf{n}^\top \dot{\mathbf{p}}_1 - (r + \|\mathbf{p}_2 - \mathbf{p}_1\|_2) \|\mathbf{n} \times \boldsymbol{\omega}\|_2 > 0. \quad (23)$$

Proof. Given a vector \mathbf{n} , we want to determine the minimal speed any point in a capsule \mathcal{C} has in the direction of \mathbf{n} as

$$\check{v}_n = \min_{\mathbf{p} \in \mathcal{C}} \mathbf{n}^\top \dot{\mathbf{p}}. \quad (24)$$

A point $\mathbf{p} \in \mathcal{C}(\mathbf{p}_1, \mathbf{p}_2, r)$ can be described as $\mathbf{p} = \mathbf{p}_1 + \lambda(\mathbf{p}_2 - \mathbf{p}_1) + \mathbf{r}$ with $\lambda \in [0, 1]$, and $\|\mathbf{r}\|_2 \leq r$. The speed of such a point in the direction of \mathbf{n} is

$$\mathbf{n}^\top \dot{\mathbf{p}} = \mathbf{n}^\top \dot{\mathbf{p}}_1 + \mathbf{n}^\top (\boldsymbol{\omega} \times (\mathbf{p} - \mathbf{p}_1)) \quad (25a)$$

$$= \mathbf{n}^\top \dot{\mathbf{p}}_1 + (\mathbf{p} - \mathbf{p}_1)^\top (\mathbf{n} \times \boldsymbol{\omega}) \quad (25b)$$

$$= \mathbf{n}^\top \dot{\mathbf{p}}_1 + \|\mathbf{p} - \mathbf{p}_1\|_2 \|\mathbf{n} \times \boldsymbol{\omega}\|_2 \cos(\alpha) \quad (25c)$$

$$\geq \mathbf{n}^\top \dot{\mathbf{p}}_1 - (r + \|\mathbf{p}_2 - \mathbf{p}_1\|_2) \|\mathbf{n} \times \boldsymbol{\omega}\|_2 = \check{v}_n, \quad (25d)$$

where α is the angle between $\mathbf{p} - \mathbf{p}_1$ and $\mathbf{n} \times \boldsymbol{\omega}$. Therefore, all points on a capsule $\mathcal{C}(\mathbf{p}_1, \mathbf{p}_2, r)$ move away from a plane with normal vector \mathbf{n} if $\check{v}_n > 0$. \square

We can only compute the velocity and acceleration of a point on the i -th robot link $\mathbf{p}_{i,1}^r$ at discrete time points using the link Jacobian \mathbf{J}_i [54, Eq. 7.16] as $\mathbf{v}_{i,1}^r = \mathbf{J}_i \dot{\mathbf{q}}$ and $\dot{\mathbf{v}}_{i,1}^r = \dot{\mathbf{J}}_i \dot{\mathbf{q}} + \mathbf{J}_i \ddot{\mathbf{q}}$. To bound the velocity error for an entire time interval, we apply Theorem V.3.

Let \mathbf{p} be a point on robot link r_i in the time interval $[t_a, t_b]$, and let $\bar{t} = \frac{t_a + t_b}{2}$. The projection of the linear velocity $\dot{\mathbf{p}}$ onto a vector \mathbf{n} can be approximated by a first-order Taylor polynomial:

$$\mathbf{v}_n^p(t) = \mathbf{v}_n^p(\bar{t}) + (\dot{\mathbf{v}}_n^p(\bar{t})) (t - \bar{t}) + r_n(t, \bar{t}), \quad (26)$$

where the Lagrange remainder r_n satisfies

$$|r_n(t, \bar{t})| \leq \sup_{\tau \in [\bar{t}, t]} \frac{1}{2} |\ddot{\mathbf{v}}_n^p(\tau)| (t - \bar{t})^2. \quad (27)$$

Theorem V.3. Using the approximation in (26), the speed of any point on the i -th robot link $\mathbf{p} \in \mathcal{C}(\mathbf{p}_{i,1}^r, \mathbf{p}_{i,2}^r, r_i^r) := \mathcal{C}_i$ projected onto the vector \mathbf{n} with $\|\mathbf{n}\|_2 = 1$ in the time interval $[t_a, t_b]$ is bounded below by:

$$\check{v}_{n,i} = \min_{\mathbf{p} \in \mathcal{C}_i, t \in [t_a, t_b]} \mathbf{v}_n^p(t) \quad (28)$$

$$\begin{aligned} &\geq \mathbf{n}^\top \dot{\mathbf{p}}_{i,1}^r - w_{v,max} - l_i (\|\mathbf{n} \times \boldsymbol{\omega}_{i,1}^r\|_2 + w_{\omega,max}) \\ &+ \frac{\Delta t}{2} \left(\mathbf{n}^\top \ddot{\mathbf{p}}_{i,1}^r - w_{a,max} - l_i (\|\mathbf{n} \times \dot{\boldsymbol{\omega}}_{i,1}^r\|_2 + \right. \\ &\quad \left. \|\boldsymbol{\omega}_{i,1}^r\|_2 \|\mathbf{n} \times \boldsymbol{\omega}_{i,1}^r\|_2 + w_{\dot{\omega},max} + \right. \\ &\quad \left. w_{\omega,max} (\|\boldsymbol{\omega}_{i,1}^r\|_2 + \|\mathbf{n} \times \boldsymbol{\omega}_{i,1}^r\|_2 + w_{\omega,max}) \right) \\ &- \frac{\Delta t^2}{8} \sum_{j=1}^i l_j \left(\hat{\omega}_j + 3\hat{\omega}_j \hat{\omega}_j + \hat{\omega}_j^2 \right), \end{aligned} \quad (29)$$

where $\Delta t = t_b - t_a$, $w_{v,max}$, $w_{\omega,max}$, $w_{a,max}$, and $w_{\dot{\omega},max}$ are the maximal absolute estimation errors of the linear and angular velocity and acceleration, and $l_i = \|\mathbf{p}_{i,2}^r - \mathbf{p}_{i,1}^r\|_2 + r_i^r$, and

$$\hat{\omega}_j := \sum_{k=1}^j \hat{q}_k, \quad (30a)$$

$$\hat{\omega}_j := \sum_{k=1}^j \hat{q}_k + \hat{q}_k \hat{\omega}_{k-1}, \quad (30b)$$

$$\hat{\omega}_j := \sum_{k=1}^j \hat{q}_k + 2\hat{q}_k \hat{\omega}_{k-1} + \hat{q}_k (\hat{\omega}_{k-1} + \hat{\omega}_{k-1}^2), \quad (30c)$$

$$l_j := \begin{cases} \|\mathbf{p}_{j,2}^r - \mathbf{p}_{j,1}^r\|_2, & j < i \\ \|\mathbf{p}_{j,2}^r - \mathbf{p}_{j,1}^r\|_2 + r_j^r, & j = i. \end{cases} \quad (30d)$$

Proof. See Appendix Sec. A. \square

Using $\check{v}_{n,i}$, we incorporate the ECC constraint in (16) into a new constraint to exclude cases, where a robot link r_i is moving away from the surface of an environment element e_k , using

$$\bar{c}_{\text{ECC},i,j,k}''([t_a, t_b]) := \bar{c}_{\text{ECC},i,j,k}'([t_a, t_b]) \wedge \bar{c}_{\text{contact},i,k}([t_a, t_b]) \bigwedge_{n \in \mathcal{N}_{i,k}} (\check{v}_{n,i} \geq 0). \quad (31)$$

Correspondingly, we define a new constraint based on the SCC constraint between two robot links r_i and r_l in (17) as

$$\bar{c}_{\text{SCC},i,j,l}''([t_a, t_b]) := \bar{c}_{\text{SCC},i,j,l}'([t_a, t_b]) \wedge \bar{c}_{\text{contact},i,l}([t_a, t_b]) \bigwedge_{n \in \mathcal{N}_{i,l}} (\check{v}_{n,i} \geq \check{v}_{n,l}). \quad (32)$$

3) *Robot Topology:* Most collaborative robots are designed to prevent clamping between certain robot links, either through their topology or by limiting the joint angles. Hence, for a given robot, we define the set of robot link pairs that cannot cause an SCC as

$$\mathcal{G}^r = \{(r_i, r_l) \mid \text{no SCC between link } r_i \text{ and } r_l \text{ possible}\} \quad (33)$$

and extend (32) by

$$\bar{c}_{\text{SCC},i,j,l}'''([t_a, t_b]) := \bar{c}_{\text{SCC},i,j,l}''([t_a, t_b]) \vee (r_i, r_l) \in \mathcal{G}^r. \quad (34)$$

4) *Full Constrained Contact Detection:* With the derived constraint relaxations, we redefine the ECC and SCC constraints in (12) and (15) as

$$\bar{c}_{\text{ECC},i,j}([t_a, t_b]) := \bigwedge_{e_k \in \mathcal{E}} \bar{c}_{\text{ECC},i,j,k}''([t_a, t_b]) \quad (35)$$

$$\bar{c}_{\text{SCC},i,j}([t_a, t_b]) := \bigwedge_{r_l \in \mathcal{R} \setminus r_i} \bar{c}_{\text{SCC},i,j,l}'''([t_a, t_b]). \quad (36)$$

C. Handling Multi-Body Clamping

An important scenario to consider is the case, where the robot clamps multiple human body parts, e.g., both hands are clamped in between the robot and a table. In these cases, the constraint in (11) does not guarantee the detection of all possible constrained contacts anymore. To handle the clamping of multiple human body parts at the same time, we combine all body parts that could be in contact with each other to a new virtual body part. Fortunately, within a human body, there are a number of body part combinations that cannot lead to critical constrained contact and can thereby be excluded, e.g., clamping the right hand and the right lower arm. Therefore, we define the set of safe human body part pairs as

$$\mathcal{G}^h = \{(h_j, h_{j'}) \mid \text{no clamping of } h_j \text{ and } h_{j'} \text{ possible} \wedge h_j \text{ and } h_{j'} \text{ belong to the same human}\}. \quad (37)$$

To find all connected body parts, we construct an undirected graph \mathbb{G} , where the vertices are the body parts $h_j \in \mathcal{H}$ of all

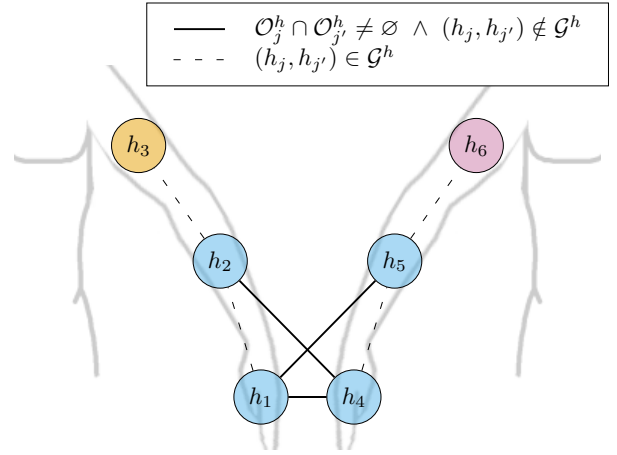


Fig. 4. Example of a simplified contact graph \mathbb{G} with two humans in the scene. All connected components in the graph are colored differently. The connected component of $\mathcal{H}_{c,1} = \{h_1, h_2, h_4, h_5\}$ is combined to a new body part and the set of all connected components is $\mathcal{H}_c = \{\mathcal{H}_{c,1}, \{h_3\}, \{h_6\}\}$.

humans in the scene. The edges between two vertices h_j and $h_{j'}$ are denoted as $\langle h_j, h_{j'} \rangle$. We construct an edge

$$\langle h_j, h_{j'} \rangle \text{ if } \mathcal{O}_j^h \cap \mathcal{O}_{j'}^h \neq \emptyset \wedge (h_j, h_{j'}) \notin \mathcal{G}^h. \quad (38)$$

Figure 4 provides an example of a simplified graph with two human arms in the scene.

We use a depth-first search algorithm [55] to find the set of all connected components² $\mathcal{H}_c \subset \mathcal{P}(\mathcal{H})$ in the graph. We construct an additional set of human body parts $\tilde{\mathcal{H}}$ by creating a new combined body part per connected component $\mathcal{H}_{c,a} \in \mathcal{H}_c : |\mathcal{H}_{c,a}| > 1$. A new combined body part $h_{\tilde{j}} \in \tilde{\mathcal{H}}$ is built from the elements in $\mathcal{H}_{c,a} \in \mathcal{H}_c$ and has a diameter, occupancy, and admissible contact energy of

$$d_{\tilde{j}}^h := \sum_{h_j \in \mathcal{H}_{c,a}} d_j^h \quad (39a)$$

$$\mathcal{O}_{\tilde{j}}^h := \bigcup_{h_j \in \mathcal{H}_{c,a}} \mathcal{O}_j^h \quad (39b)$$

$$T_{\text{clamp},i,\tilde{j}} := \min_{h_j \in \mathcal{H}_{c,a}} T_{\text{clamp},i,j}. \quad (39c)$$

We guarantee the safety for these combined body parts by rewriting the constraints in (4) and (10) to the new constraint

$$c'_{\text{safe}}(\chi_M) := c_{\text{safe}}(\chi_M) \bigwedge_{a=0}^{M-1} \bigwedge_{r_i \in \mathcal{R}} \bigwedge_{h_{\tilde{j}} \in \tilde{\mathcal{H}}} \bar{c}_{\text{contact},i,\tilde{j}}([t_a, t_{a+1}]) \vee c_{\text{free},i,\tilde{j}}([t_a, t_{a+1}]) \vee c_{T,\text{clamp},i,\tilde{j}}([t_a, t_{a+1}]). \quad (40)$$

Note, that we do not verify the unconstrained contact energy for the combined body parts in (40) as these are already verified for the individual bodies in $c_{\text{safe}}(\chi_M)$. In Appendix Sec. B we show that if (40) holds for a combined body part, it also holds for all constrained contacts involving all possible combinations of body parts in that combined body part.

TABLE I
ADMISSIBLE CONTACT ENERGIES.

Body Part	Robot Geometry	Constrained Contact $T_{\text{clamp},i,j}$ [J]				Unconstrained Contact $T_{\text{free},i,j}$ [J]			
		Blunt [†]	Wedge [*]	Edge [*]	Sheet [*]	Blunt [†]	Wedge [‡]	Edge [‡]	Sheet [‡]
Hand		0.49	0.05	0.02	0.11	0.49	2.0	0.375	0.9
Lower Arm		1.3	0.05	0.02	0.11	1.3	2.0	0.375	0.9
Upper Arm		1.5	0.05	0.02	0.11	1.5	0.5	0.2	0.5
Torso (Chest)		1.6	0.05	0.02	0.11	1.6	0.5	0.2	0.5
Head (Face)		0.11	0.05	0.02	0.11	0.11	0.11 [†]	0.11 [†]	0.11 [†]

[†]From [17], ^{*}From [40], [‡]From [16]

VI. CONTACT ENERGY CONSTRAINTS

This section discusses how we evaluate the contact energy constraints $c_{T,\text{free},i,j}$ and $c_{T,\text{clamp},i,j}$ in (40). For this, we derive the effective kinetic energy of the robot with respect to a contact with robot link r_i in a given configuration and define the necessary constraints for all possible contacts.

The kinetic energy of the entire robot is [54, Eq. 7.31]

$$T^r(\mathbf{q}) = \frac{1}{2} \dot{\mathbf{q}}^\top \mathbf{B}(\mathbf{q}) \dot{\mathbf{q}}, \quad (41)$$

where $\mathbf{B}(\mathbf{q})$ is the inertia matrix. In this work, we assume that the robot consists of rigid body parts without joint elasticity, where the motor masses and inertia are included in the links, so we can formulate the inertia matrix as [54, Eq. 7.32]

$$\mathbf{B}(\mathbf{q}) = \sum_{i=1}^N m_i \mathbf{J}_i^P \mathbf{J}_i^P + \mathbf{J}_i^{O\top} \mathbf{R}_i \mathbf{I}_i \mathbf{R}_i^\top \mathbf{J}_i^O, \quad (42)$$

where m_i is the mass of link r_i , \mathbf{J}_i^P and \mathbf{J}_i^O are the i -th link Jacobians [54, Eq. 7.16] with respect to the position and orientation, \mathbf{R}_i is the rotation matrix from the i -th link frame to the base frame, and \mathbf{I}_i is the inertia tensor of link r_i .

We show that the effective kinetic energy of the robot with respect to a point on link $i < N$ is independent of the rotational velocity of the joints $i + 1, \dots, N$. Let \mathbf{p}_i^r be a point on link r_i . The motion of \mathbf{p}_i^r only depends on the joint velocities q_1, \dots, q_i , i.e.,

$$\mathbf{v}_i^r = \mathbf{J}_i \mathbf{E}_i \dot{\mathbf{q}} \quad (43)$$

where \mathbf{J}_i is the Jacobian with respect to the point \mathbf{p}_i^r and \mathbf{E}_i is the truncated identity matrix with 1s on the diagonal up to row i and 0s elsewhere. The effective kinetic energy of the robot with respect to a point \mathbf{p}_i^r is given in [27, Sec. 2] as

$$T_i^r(\mathbf{q}) = \frac{1}{2} \mathbf{v}_i^{r\top} \Lambda_i(\mathbf{q}) \mathbf{v}_i^r, \quad (44)$$

where

$$\Lambda_i(\mathbf{q}) = (\mathbf{J}_i^\top)^{-1} \mathbf{B}(\mathbf{q}) (\mathbf{J}_i)^{-1} \quad (45)$$

is the operational space kinetic energy matrix from [27, Eq. 2]. Inserting (43) and (45) into (44) directly leads to the effective

kinetic energy exerted upon contact with a point on the robot link r_i as

$$T_i^r(\mathbf{q}) = \frac{1}{2} \dot{\mathbf{q}}^\top \mathbf{E}_i \mathbf{B}(\mathbf{q}) \mathbf{E}_i \dot{\mathbf{q}}. \quad (46)$$

Thus, we define the contact energy constraints in (10) as

$$c_{T,\text{free},i,j}([t_a, t_b]) = \max(T_i^r(\mathbf{q}(t_a)), T_i^r(\mathbf{q}(t_b))) < T_{\text{free},i,j} \quad (47)$$

$$c_{T,\text{clamp},i,j}([t_a, t_b]) = \max(T_i^r(\mathbf{q}(t_a)), T_i^r(\mathbf{q}(t_b))) < T_{\text{clamp},i,j}, \quad (48)$$

where $T_{\{\text{type}\},i,j}$ gives the maximal contact energy for the respective human body part, contact type, and link index. We list all contact energies used in SARA shield in Table I. For the torso and head, we use the chest and face thresholds of ISO/FDIS 10218-2:2024 as they are more conservative than the abdomen and skull values. The link index is included in this threshold so that we can differentiate between different worst-case contact shapes on the different links. For most collaborative robots the first $N - 1$ links are designed to only induce blunt contacts, whereas the worst-case impact shape on the end effector depends on the gripper and tool. For the limits in Table I, we assume that the human skin is similar to dew claws, as discussed in [16, Sec. III-A]. The constrained contact energies for the head are taken from [17, Tab. M.4], which already proposes conservative values.

VII. EXPERIMENTS

This section tests our two main hypotheses:

- H1** SARA shield significantly improves the robot performance in comparison to previous safe HRC approaches.
- H2** The kinetic energy of a robot controlled with SARA shield during a contact with a human is below injury thresholds.

We evaluate **H1** in Sec. VII-A and **H2** in Sec. VII-B. All experiments were conducted on a Schunk LWA 4P robot.

A. Robot Efficiency Evaluation

In this subsection, we evaluate **H1** in simulation using recorded human motions in Sec. VII-A1 and on a real HRC setup in Sec. VII-A2.

²A connected component is a set of vertices where each vertex is reachable from any other vertex in the set, and no additional vertices can be added while preserving this property.

TABLE II
MEAN AND STANDARD DEVIATION OF THE ROBOT EFFICIENCY ACROSS 30 TRIALS.

Method	Efficiency per End Effector Type [%]		p-value of H1	Computation Time [ms]	Provably safe w.r.t. Sec. III-D
	Blunt	Sharp			
SSM zone [56]	6.8 ± 10.7	6.8 ± 10.7	8.14e-12	0.09 ± 0.01	✓
Reduced-speed PFL [56]	38.5 ± 8.5	38.5 ± 8.5	8.14e-12	0.12 ± 0.02	✗
Dynamic SSM [12, 19]	59.2 ± 19.7	59.2 ± 19.7	8.14e-12	0.15 ± 0.04	✓
Reduced-speed zone [7]	64.5 ± 13.8	64.5 ± 13.8	8.14e-12	0.22 ± 0.04	✗
Reflected mass [11]	83.4 ± 3.4	80.4 ± 4.7	1.10e-11	1.00 ± 5.02	✗
SARA shield without c_{free}	82.3 ± 13.1	82.3 ± 7.8	8.15e-12	0.36 ± 0.05	✓
SARA shield (ours)	92.6 ± 6.3	92.5 ± 6.2	–	0.41 ± 0.29	✓

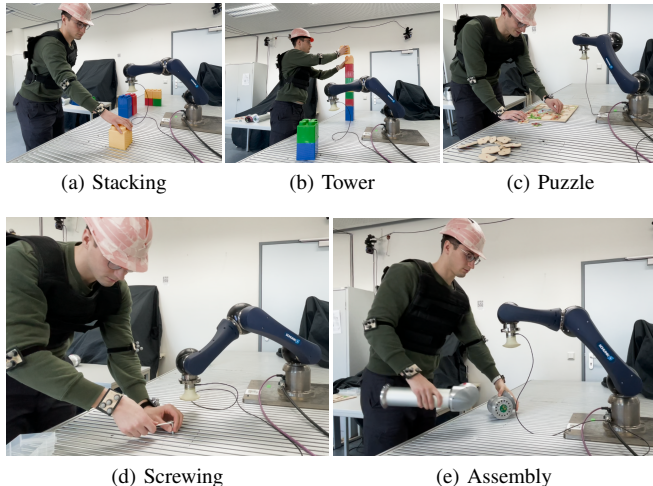


Fig. 5. The five HRC tasks evaluated in our ablation study.

1) *Simulated Robot Efficiency Study*: To fairly compare the robot efficiency across different methods, we gathered a dataset of human motion capture data in our lab while the robot was stopped³. For this, we defined the five tasks depicted in Fig. 5, which require close collaboration between the human and the robot and should emulate typical real-world tasks:

- **Stacking**: the user has to stack two 10×10×10 cm blocks in multiple pre-defined positions.
- **Tower**: the user has to stack eight 10×10×10 cm blocks to a tower at two pre-defined positions.
- **Puzzle**: the user has to solve a simple puzzle.
- **Screwing**: the user has to screw ten screws into random positions using an allen wrench.
- **Assembly**: the user has to assemble two modules of a modular robot of the company RobCo.

All tasks were performed for three minutes in the robot workspace, and the task was repeated if finished early. We collected data from six participants with a randomized order of tasks, leading to a total number of 30 trials.

For all tasks, the robot trajectory emulates a typical pick and place motion, where the robot approaches two pre-

³This study is exempt from ethics review because it involved non-invasive motion capture of adult participants performing standard movements in a laboratory setting. No personal or identifiable information was collected, participation was voluntary and without compensation, and no interventions or sensitive questions were involved.

defined positions on the table located on the outer edges of the combined human and robot workspace. This trajectory contains both potential high-speed unconstrained contacts and constrained contacts with the table. Our supplementary video further visualizes these five tasks and the robot trajectory.

We simulate the robot behavior given the human measurements from the motion capture recordings across eight different methods, all of which are available in our open-source code release:

- **No shield**: the robot executes its trajectory at full speed.
- **SSM zone**: if any body part is closer than 1.17 m to the robot base, we stop the robot. This represents the separation distance speed and separation monitoring approach in ISO/FDIS 10218-2:2024, and the threshold is calculated according to [7, Eq. 7].
- **Reduced-speed PFL**: the maximal Cartesian speed of the robot is limited to 0.25 m s⁻¹ representing the reduced-speed power and force limiting approach in ISO/FDIS 10218-2:2024⁴.
- **Dynamic SSM**: we use the set-based reachability speed and separation monitoring method of [12, 19] that stops the robot at the latest possible moment.
- **Reduce speed zone**: we follow the approach of [7] and let the robot operate at full speed if the human is far away and switch to reduced-speed PFL if any body part is closer than 0.73 m to the robot base⁴.
- **Reflected mass**: the reflected mass method proposed by Haddadin et al. [11], where we adapt their safe motion unit velocities to match our energy limits in Table I, ensuring a fair comparison. Since this approach has no contact type classification, we are using the more conservative constrained contact thresholds⁵.
- **SARA shield without c_{free}** : our approach without contact type classification, where we use the more conservative constrained contact thresholds for all possible contacts.
- **SARA shield**: our proposed method with contact type classification and contact energy reduction.

In Table II, we report the mean and standard deviation of the percentage of the total trajectory covered by each method in relation to the execution of the **no shield** method. This metric can be interpreted as the task completion percentage

⁴This approach does not guarantee safety for all robot masses and sharp robot geometries.

⁵This approach assumes a static human for the reflected mass calculation.

of the collaborative robot and directly evaluates the robot efficiency. We report the results for the blunt and sharp end effector geometries, where sharp contains edge, sheet, and wedge shapes to equal parts.

The results clearly show that SARA shield outperforms all baseline methods in terms of robot efficiency. To make statistically significant claims, we compute the robot efficiency differences per trial and end effector type of all methods to SARA shield. Our null hypothesis is that the efficiency values of the baseline method and the ones of SARA shield come from the same distribution, and the alternative hypothesis is **H1**. For all methods, a Shapiro-Wilk test for normality [57] indicates that the efficiency difference data is not normally distributed across the trials. Hence, we perform a Wilcoxon signed-rank test [58] to compute the statistical significance of **H1** across all baseline methods. The p-values in Table II show a very strong statistical evidence for **H1**. In fact, for all but one trial in the comparison with the reflected mass method, SARA shield performed strictly better than the baseline methods.

Our evaluation further shows that our proposed contact type classification has a strong impact on the overall robot performance. Without this method, our approach performs similar to that of Haddadin et al. [11] with the major difference that we do not assume a static human for our contact energy thresholds. We further see that the end effector type does not have a strong impact on the robot efficiency for SARA shield as most contact situations are unconstrained, where all end effector types permit a relatively high robot energy.

Table II further reports the average runtime of the methods in our custom implementation⁶. Note, that we focused our implementation of the state-of-the-art methods on a fair comparability of the robot efficiency rather than runtime efficiency. The computational overhead of SARA shield is not drastically higher than related methods and all methods are real-time deployable.

We further provide an assessment whether the methods provide provable human safety with respect to (w.r.t.) our assumption in Sec. III-D. The reduced-speed PFL approach in [56] and the reduced-speed zone approach in [7] are not provably safe for sharp robot geometries as even light-weight robots with sharp contacts can inflict injuries at 0.25 m s^{-1} [40]. Since Haddadin et al. [11] assume a stationary human for their verification, their reflected mass approach violates our assumption that humans can move with up to 1.6 m s^{-1} in any direction.

2) *Real-World HRC Evaluation*: To demonstrate the performance of SARA shield, we compare its real-world behavior with the speed and separation monitoring approach in [12, 19] (dynamic SSM). For this, we deploy both methods on a Schunk LWA 4P robot controlled by a speedgoat real-time target machine at a control frequency of 166.7 Hz. The user performs the collaborative tasks described in Sec. VII-A in the workspace of the moving robot. For this experiment, we set the end effector geometry to the edge type.

The performance difference of SARA shield and the dynamic SSM approach is best visualized in our supplementary

video. Here, we can see that the robot operated with SARA shield only has to slow down negligibly when moving from one pick location to another (unconstrained contact). The dynamic SSM robot comes to a full stop or slows down significantly in these cases. When a constrained contact is possible, our approach allows the robot to continue operation with a safe speed, whereas the dynamic SSM robot has to come to a full stop and wait for the user to clear the area.

To also give a quantitative analysis of this deployment, we again record the human motion and compare the executed robot path with a simulated execution without safety shield⁷. Hereby, the robot operated with SARA shield achieves a relative performance of $93.7 \pm 4.9\%$ and the dynamic SSM robot falls short with a performance of $55.9 \pm 19.2\%$. These findings align with the results of Table II, showing that the performance does not differ significantly when the user is aware of the robot. These findings further support the validity of **H1**.

B. Contact Energy Evaluation

To evaluate **H2**, we conduct collision experiments for constrained contacts in Sec. VII-B1 and for unconstrained contacts in Sec. VII-B2.

1) *Constrained Contact Validation*: ISO/FDIS 10218-2:2024 and ISO/TS 15066 [59] specify admissible contact forces given blunt robot geometries and reference stiffness values for all human body parts. The goal of this subsection is to validate if a robot controlled with SARA shield adheres to these force limits in constrained contacts. For this, we measure the contact forces of the robot during a constrained contact with a Pilz robot measurement system, which is certified for ISO/TS 15066 [59] and emulates varying contact stiffness. During our tests, we manually set the human pose measurements so that the human body part under test is located at the sensor location and a constrained contact is detected.

To this date, no ISO norm specifies force limits for sharp contacts. However, they provide a formula to convert the contact energy into a maximal transient contact force [17, Eq. M.1]

$$F_{\text{clamp},i,j} = \sqrt{2K_j^h T_{\text{clamp},i,j}}, \quad (49)$$

where K_j^h is the reference stiffness of the human body part. We use (49) to convert the contact energies in Table I to admissible force limits for all end effector geometries, and perform five force measurements per end effector geometry (edge, wedge, sheet, and blunt) and human body part modeled in SARA shield (hand, lower arm, upper arm, chest, and face).

Since the primary purpose of this article is to derive a framework that effectively limits the transient contact forces, we deploy a simple contact reaction scheme using an external force sensor mounted on the end effector to limit the quasi-static forces. Our contact reaction scheme reacts within 100 ms, which aligns with recently proposed methods using internal joint torque or current measurements [5, 6, 60].

⁷A real-world deployment without safety shield would not be safe, so we did not gather real-world collaborative data for this setting.

⁶Executed single-thread on an Intel © Core © i7-10750H @ 2.60GHz.

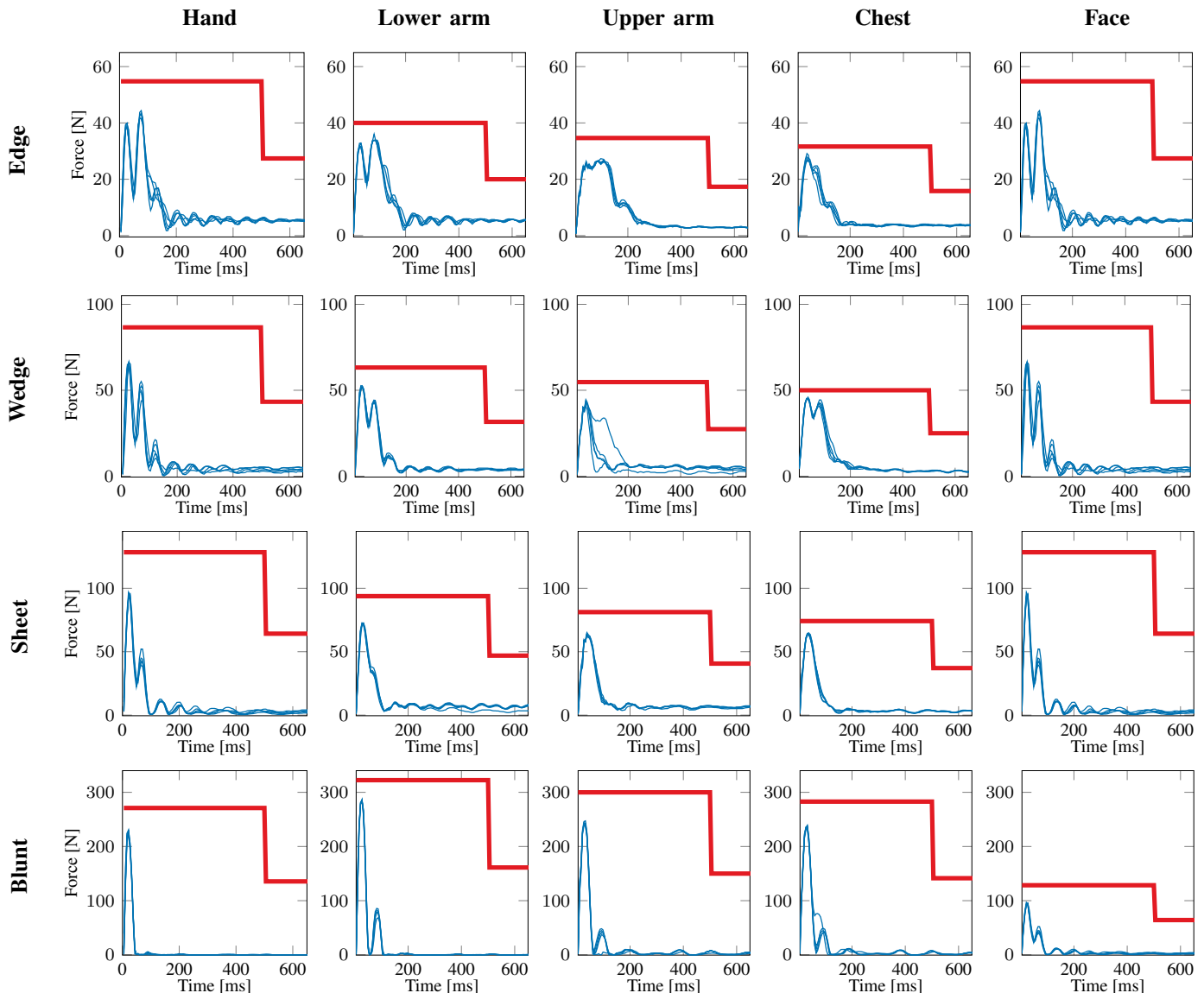


Fig. 6. Force measurements for the Schunk robot using the Pilz robot measurement system for varying body parts (columns) and end effector types (rows). The admissible force limits are depicted in red and the measured forces across five measurements in blue. The force limits in rows one to three are derived from the energy limits in Table I using (49) and the limit in row four is from ISO/FDIS 10218-2:2024.

The results in Fig. 6 show that SARA shield successfully limits the transient contact forces to the given limits for all end effector geometries and human body parts. We report that no force measurement exceeds the respective force limit, which confirms **H2** for constrained contacts.

2) *Unconstrained Contact Validation*: To validate that the kinetic energy of the robot is below the unconstrained contact energy thresholds in Table I, we set up an experiment where the robot collides with a pendulum at different speeds, as depicted in Fig. 7. The robot moves along a trajectory such that the normal vector of the contact is perpendicular to the rotation axis of the pendulum. The end effector and pendulum are stiff, so we assume there is an elastic contact between them. Upon contact, the pendulum swings backward, and the robot stops once the contact is detected by the external sensor as described in the previous subsection.

We measure the position of the pendulum with a motion-

tracking system and calculate the maximum height of its center of mass in the swing-back motion using simple trigonometry. Using the height measurement and the known pendulum mass, we can determine the potential energy of the pendulum at its peak $T_{\text{pot}} = m_{\text{pendulum}} g \Delta z_{\text{COM}}$, where $g = 9.81 \text{ m s}^{-2}$. As the friction in the pendulum is negligible, we assume that the kinetic energy of the pendulum after the contact equals its peak potential energy. Due to the law of conservation of energy, the kinetic energy of the robot at the time of contact can never exceed the potential energy of the pendulum.

In our pendulum experiment, we define the energy thresholds $T_{\text{free}} = [0.1 \text{ J}, 0.25 \text{ J}, 0.4 \text{ J}, 0.55 \text{ J}, 0.7 \text{ J}]$ of SARA shield and emulate a human body part h_j positioned at the contact point. For each energy value, we let the robot collide with a pendulum of increasing mass $m_{\text{pendulum}} = [1.132 \text{ kg}, 2.132 \text{ kg}, 3.132 \text{ kg}, 4.132 \text{ kg}, 5.132 \text{ kg}, 6.132 \text{ kg}]$,

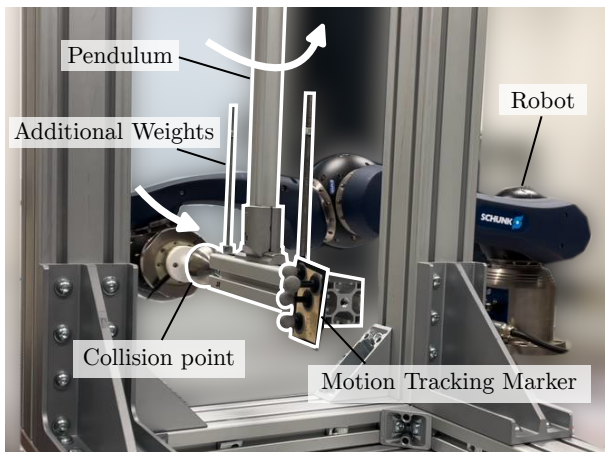


Fig. 7. The pendulum experiment setup. The robot end effector collides with the pendulum, causing it to swing backwards. A Vicon motion tracking system measures the position of the pendulum. The mass of the pendulum can be increased by adding weights to the two rods. The robot stops at the point of contact.

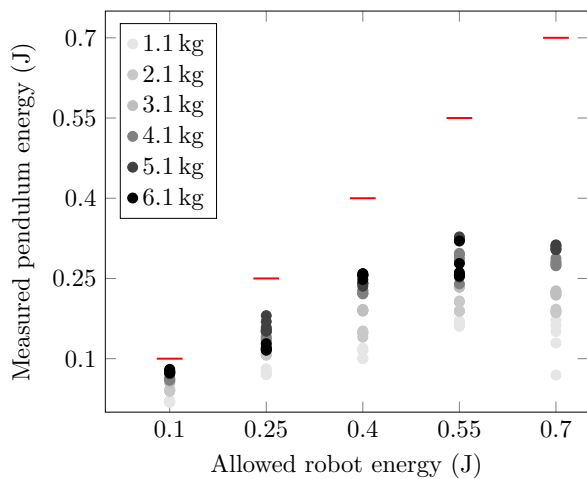


Fig. 8. Results of the kinetic energy validation using a pendulum setup for varying pendulum masses. All measured pendulum energies are below the set maximal threshold of SARA shield⁸.

with five contacts per mass value⁸. The calculated reflected mass [27] of the robot at the contact point is 4.261 kg, so these pendulum masses cover a range including the robot mass. These masses also cover the typical effective masses of the human arm given in ISO/FDIS 10218-2:2024, which are 0.6 kg for the hand, 2.6 kg for the forearm, and 5.6 kg for the entire arm.

The results in Fig. 8 show that the measured pendulum energy does not exceed the maximal allowed kinetic energy during contact for all masses. This supports the validity of **H2** for unconstrained contacts. For higher velocities, the measured energy was strongly below the allowed contact energy, which might indicate that our assumption of an elastic contact is incorrect. Nevertheless, the kinetic energy induced in the contact is lower than the respective limits, which would be safe for all human contacts.

⁸We left out the mass of 6.132 kg for the highest energy of 0.7 J to prevent damage to the robot hardware.

VIII. CONCLUSION

SARA shield is the first provably safe power and force limiting approach that ensures safe contact energies for different body parts, sharp robot geometries, and dynamic human motion. Our approach is certifiable as it incorporates time and measurement delays for all human and robot motion and ensures safety through formal methods. In comparison to previous work, we do not assume a static human or simply verify against the most conservative force limit. In extensive experimental evaluations, our approach significantly improved the robot performance over all state-of-the-art approaches. The key methodology enabling this non-conservative behavior is classifying contacts by their type, as unconstrained contacts permit a significantly higher contact energy than constrained contacts. With the significant improvements to robot performance in close HRC, SARA shield will accelerate the deployment of autonomous agents in critical human environments. Future work aims at extending our framework to mobile manipulators and humanoid robots, with a particular focus on operational-space control.

APPENDIX A

DERIVATION OF VELOCITY ERROR

In this section, we prove Theorem V.3. Throughout this section, we use the relations

$$\mathbf{a}^\top (\mathbf{b} + \mathbf{c}) = \mathbf{a}^\top \mathbf{b} + \mathbf{b}^\top \mathbf{c} \quad (50)$$

$$\mathbf{a} \times (\mathbf{b} + \mathbf{c}) = \mathbf{a} \times \mathbf{b} + \mathbf{b} \times \mathbf{c} \quad (51)$$

$$\mathbf{a}^\top (\mathbf{b} \times \mathbf{c}) = \mathbf{b}^\top (\mathbf{c} \times \mathbf{a}) = \mathbf{c}^\top (\mathbf{a} \times \mathbf{b}) \quad (52)$$

$$\|\mathbf{p} - \mathbf{p}_{i,1}^r\|_2 \leq \|\mathbf{p}_{i,2}^r - \mathbf{p}_{i,1}^r\|_2 + r_i^r \stackrel{(30d)}{=} l_i \quad (53)$$

$$\|\mathbf{a} \times \mathbf{b}\|_2 = \|\mathbf{a}\|_2 \|\mathbf{b}\|_2 \sin(\theta) \leq \|\mathbf{a}\|_2 \|\mathbf{b}\|_2 \quad (54)$$

$$\mathbf{a}^\top \mathbf{b} = \|\mathbf{a}\|_2 \|\mathbf{b}\|_2 \cos(\theta) \geq -\|\mathbf{a}\|_2 \|\mathbf{b}\|_2 \quad (55)$$

to derive this proof, where θ is the angle between the vectors \mathbf{a} and \mathbf{b} .

Proof. We derive the approximation in three parts:

$$\check{v}_{n,i} = \min_{\mathbf{p} \in \mathcal{C}_i, t \in [t_a, t_b]} v_n^p(t) \quad (56)$$

$$\stackrel{(26)}{\geq} \underbrace{\min_{\mathbf{p} \in \mathcal{C}_i} v_n^p(\bar{t})}_I + \underbrace{\frac{\Delta t}{2} \min_{\mathbf{p} \in \mathcal{C}_i} \dot{v}_n^p(\bar{t})}_{II} - \underbrace{\frac{\Delta t^2}{8} \max_{\mathbf{p} \in \mathcal{C}_i, t \in [t_a, t_b]} |\ddot{v}_n^p(t)|}_{III} \quad (57)$$

The relation in (57) follows trivially from the subadditivity property of the minimum operator. In the following paragraphs, we show the under-approximations for I, II and III.

a) *Lower bound of I:* We under-approximate I as

$$v_n^p = \mathbf{n}^\top \dot{\mathbf{p}} \quad (58a)$$

$$\stackrel{[54, \text{Eq. 3.26}]}{\geq} \mathbf{n}^\top (\dot{\mathbf{p}}_{i,1}^r + \mathbf{w}_v + (\boldsymbol{\omega}_i^r + \mathbf{w}_\omega) \times (\mathbf{p} - \mathbf{p}_{i,1}^r)) \quad (58b)$$

$$\stackrel{(25d)}{\geq} \mathbf{n}^\top \dot{\mathbf{p}}_{i,1}^r - w_{v, \max} - l_i (\|\mathbf{n} \times \boldsymbol{\omega}_i^r\|_2 + w_{\omega, \max}). \quad (58c)$$

b) *Lower bound of II:* Similarly to (25d), we express the velocity of any point on the i -th robot capsule $\mathbf{p} \in \mathcal{C}_i$ in relation to the first of the defining points of that capsule $\mathbf{p}_{i,1}^r$ with

$$\dot{\mathbf{v}}_{\mathbf{n}}^{\mathbf{p}} = \mathbf{n}^\top \ddot{\mathbf{p}} \quad (59a)$$

$$\stackrel{[54, \text{Eq. 7.99}]}{=} \mathbf{n}^\top (\ddot{\mathbf{p}}_{i,1}^r + \mathbf{w}_a + (\dot{\boldsymbol{\omega}}_i^r + \mathbf{w}_{\dot{\omega}}) \times (\mathbf{p} - \mathbf{p}_{i,1}^r) + (\boldsymbol{\omega}_i^r + \mathbf{w}_\omega) \times ((\boldsymbol{\omega}_i^r + \mathbf{w}_\omega) \times (\mathbf{p} - \mathbf{p}_{i,1}^r))) \quad (59b)$$

$$\stackrel{(50),(52)}{=} \mathbf{n}^\top (\ddot{\mathbf{p}}_{i,1}^r + \mathbf{w}_a) + (\mathbf{p} - \mathbf{p}_{i,1}^r)^\top (\mathbf{n} \times (\dot{\boldsymbol{\omega}}_i^r + \mathbf{w}_{\dot{\omega}})) + ((\boldsymbol{\omega}_i^r + \mathbf{w}_\omega) \times (\mathbf{p} - \mathbf{p}_{i,1}^r))^\top (\mathbf{n} \times (\boldsymbol{\omega}_i^r + \mathbf{w}_\omega)) \quad (59c)$$

$$\stackrel{(50),(51)}{=} \mathbf{n}^\top \ddot{\mathbf{p}}_{i,1}^r + \mathbf{n}^\top \mathbf{w}_a + (\mathbf{p} - \mathbf{p}_{i,1}^r)^\top ((\mathbf{n} \times \dot{\boldsymbol{\omega}}_i^r) + (\mathbf{n} \times \mathbf{w}_{\dot{\omega}})) + (\boldsymbol{\omega}_i^r \times (\mathbf{p} - \mathbf{p}_{i,1}^r))^\top ((\mathbf{n} \times \boldsymbol{\omega}_i^r) + (\mathbf{n} \times \mathbf{w}_\omega)) + (\mathbf{w}_\omega \times (\mathbf{p} - \mathbf{p}_{i,1}^r))^\top ((\mathbf{n} \times \boldsymbol{\omega}_i^r) + (\mathbf{n} \times \mathbf{w}_\omega)) \quad (59d)$$

$$\stackrel{(54),(55)}{\geq} \mathbf{n}^\top \ddot{\mathbf{p}}_{i,1}^r - w_{a,\max} - \|\mathbf{p} - \mathbf{p}_{i,1}^r\|_2 (\|\mathbf{n} \times \dot{\boldsymbol{\omega}}_i^r\|_2 + w_{\dot{\omega},\max} + \|\boldsymbol{\omega}_i^r\|_2 (\|\mathbf{n} \times \boldsymbol{\omega}_i^r\|_2 + w_{\omega,\max}) + w_{\omega,\max} (\|\mathbf{n} \times \boldsymbol{\omega}_i^r\|_2 + w_{\omega,\max})) \quad (59e)$$

$$\stackrel{(53)}{=} \mathbf{n}^\top \ddot{\mathbf{p}}_{i,1}^r - w_{a,\max} - l_i (\|\mathbf{n} \times \dot{\boldsymbol{\omega}}_i^r\|_2 + \|\boldsymbol{\omega}_i^r\|_2 \|\mathbf{n} \times \boldsymbol{\omega}_i^r\|_2 + w_{\dot{\omega},\max} + w_{\omega,\max} (\|\boldsymbol{\omega}_i^r\|_2 + \|\mathbf{n} \times \boldsymbol{\omega}_i^r\|_2 + w_{\omega,\max})), \quad (59f)$$

which provides the limit for II in (57).

c) *Lower bound of III:* We aim to derive a time-independent solution for the Lagrangian remainder that holds for all possible joint angles, velocities, accelerations, and jerks. The absolute value of the jerk of any point projected onto a normal vector \mathbf{n} is smaller or equal to its absolute jerk

$$|\ddot{v}_{\mathbf{n}}^{\mathbf{p}}| = |\mathbf{n}^\top \ddot{\mathbf{p}}| \leq \|\ddot{\mathbf{p}}\|_2. \quad (60)$$

The acceleration of a point \mathbf{p}_i^r on link r_i is provided in [54, Eq. 7.99] as

$$\ddot{\mathbf{p}}_i^r = \ddot{\mathbf{p}}_{i-1}^r + \dot{\boldsymbol{\omega}}_i^r \times \mathbf{r}_{i-1,i} + \boldsymbol{\omega}_i^r \times (\boldsymbol{\omega}_i^r \times \mathbf{r}_{i-1,i}), \quad (61)$$

where joint i is located at \mathbf{p}_{i-1}^r , $\boldsymbol{\omega}_i^r$ is the angular velocity of the i -th link, and $\mathbf{r}_{i-1,i} = \mathbf{p}_i^r - \mathbf{p}_{i-1}^r$. The jerk of this point is

$$\begin{aligned} \ddot{\mathbf{p}}_i^r &= \ddot{\mathbf{p}}_{i-1}^r + \dot{\boldsymbol{\omega}}_i^r \times \mathbf{r}_{i-1,i} + \dot{\boldsymbol{\omega}}_i^r \times \dot{\mathbf{r}}_{i-1,i} \\ &\quad + \dot{\boldsymbol{\omega}}_i^r \times (\boldsymbol{\omega}_i^r \times \mathbf{r}_{i-1,i}) \\ &\quad + \boldsymbol{\omega}_i^r \times (\dot{\boldsymbol{\omega}}_i^r \times \mathbf{r}_{i-1,i} + \boldsymbol{\omega}_i^r \times \underbrace{\dot{\mathbf{r}}_{i-1,i}}_{\stackrel{[54, \text{Eq. 3.24}]}{=} \boldsymbol{\omega}_i^r \times \mathbf{r}_{i-1,i}}) \end{aligned} \quad (62)$$

$$\stackrel{(51)}{=} \ddot{\mathbf{p}}_{i-1}^r + \dot{\boldsymbol{\omega}}_i^r \times \mathbf{r}_{i-1,i} + 2\dot{\boldsymbol{\omega}}_i^r \times (\boldsymbol{\omega}_i^r \times \mathbf{r}_{i-1,i}) + \boldsymbol{\omega}_i^r \times (\dot{\boldsymbol{\omega}}_i^r \times \mathbf{r}_{i-1,i} + \boldsymbol{\omega}_i^r \times (\boldsymbol{\omega}_i^r \times \mathbf{r}_{i-1,i})). \quad (63)$$

We use (54) to derive an upper limit for the absolute jerk

$$\|\ddot{\mathbf{p}}_i^r\|_2 \leq \|\ddot{\mathbf{p}}_{i-1}^r\|_2 + \|\mathbf{r}_{i-1,i}\|_2 (\|\dot{\boldsymbol{\omega}}_i^r\|_2 + 3\|\boldsymbol{\omega}_i^r\|_2 \|\dot{\boldsymbol{\omega}}_i^r\|_2 + \|\boldsymbol{\omega}_i^r\|_2^2). \quad (64)$$

The angular velocity and acceleration of the i -th link are provided in [54, Eq. 3.25 and Eq. 7.96] as

$$\boldsymbol{\omega}_i^r = \boldsymbol{\omega}_{i-1}^r + \dot{\mathbf{q}}[i] \mathbf{z}_{i-1}, \quad (65)$$

$$\dot{\boldsymbol{\omega}}_i^r = \dot{\boldsymbol{\omega}}_{i-1}^r + \ddot{\mathbf{q}}[i] \mathbf{z}_{i-1} + \dot{\mathbf{q}}[i] \boldsymbol{\omega}_{i-1}^r \times \mathbf{z}_{i-1}, \quad (66)$$

where \mathbf{z}_{i-1} is the rotation axis of the i -th joint and $\|\mathbf{z}_{i-1}\|_2 = 1$. The angular jerk is

$$\begin{aligned} \ddot{\boldsymbol{\omega}}_i^r &= \ddot{\boldsymbol{\omega}}_{i-1}^r + \ddot{\mathbf{q}}[i] \mathbf{z}_{i-1} + \ddot{\mathbf{q}}[i] \dot{\mathbf{z}}_{i-1} \\ &\quad + (\ddot{\mathbf{q}}[i] \boldsymbol{\omega}_{i-1}^r + \dot{\mathbf{q}}[i] \dot{\boldsymbol{\omega}}_{i-1}^r) \times \mathbf{z}_{i-1} \\ &\quad + \dot{\mathbf{q}}[i] \boldsymbol{\omega}_{i-1}^r \times \underbrace{\dot{\mathbf{z}}_{i-1}}_{\stackrel{[54, \text{Eq. 7.96}]}{=} \boldsymbol{\omega}_{i-1}^r \times \mathbf{z}_{i-1}} \end{aligned} \quad (67)$$

$$\stackrel{(51)}{=} \ddot{\boldsymbol{\omega}}_{i-1}^r + \ddot{\mathbf{q}}[i] \mathbf{z}_{i-1} + 2\dot{\mathbf{q}}[i] \boldsymbol{\omega}_{i-1}^r \times \mathbf{z}_{i-1} + \dot{\mathbf{q}}[i] (\dot{\boldsymbol{\omega}}_{i-1}^r \times \mathbf{z}_{i-1} + \boldsymbol{\omega}_{i-1}^r \times (\boldsymbol{\omega}_{i-1}^r \times \mathbf{z}_{i-1})). \quad (68)$$

Using the joint velocity, acceleration, and jerk limits, we derive limits for the angular velocity, acceleration, and jerk as

$$\|\boldsymbol{\omega}_i^r\|_2 \stackrel{(65)}{\leq} \|\boldsymbol{\omega}_{i-1}^r\|_2 + |\dot{\mathbf{q}}[i]| \quad (69)$$

$$\leq \sum_{j=1}^i \hat{q}_j = \hat{\omega}_i,$$

$$\|\dot{\boldsymbol{\omega}}_i^r\|_2 \stackrel{(66)}{\leq} \|\dot{\boldsymbol{\omega}}_{i-1}^r\|_2 + |\ddot{\mathbf{q}}[i]| + |\dot{\mathbf{q}}[i]| \|\boldsymbol{\omega}_{i-1}^r\|_2 \quad (70)$$

$$\leq \sum_{j=1}^i \hat{q}_j + \hat{q}_j \hat{\omega}_{j-1} = \hat{\omega}_i,$$

$$\|\ddot{\boldsymbol{\omega}}_i^r\|_2 \stackrel{(68)}{\leq} \|\ddot{\boldsymbol{\omega}}_{i-1}^r\|_2 + |\ddot{\mathbf{q}}[i]| + 2|\dot{\mathbf{q}}[i]| \|\boldsymbol{\omega}_{i-1}^r\|_2 + |\dot{\mathbf{q}}[i]| (\|\dot{\boldsymbol{\omega}}_{i-1}^r\|_2 + \|\boldsymbol{\omega}_{i-1}^r\|_2^2) \quad (71)$$

$$\leq \sum_{j=1}^i \hat{q}_j + 2\hat{q}_j \hat{\omega}_{j-1} + \hat{q}_j (\hat{\omega}_{j-1} + \hat{\omega}_{j-1}^2) = \hat{\omega}_i.$$

Using these limits, we can bound the jerk of a point $\mathbf{p} \in \mathcal{C}_i$ on the i -th link to

$$\|\ddot{\mathbf{p}}\|_2 \stackrel{(64),(69),(70),(71)}{\leq} \sum_{j=1}^i l_j (\hat{\omega}_j + 3\hat{\omega}_j \hat{\omega}_j + \hat{\omega}_j^2), \quad (72)$$

where the lengths l_j are given in (30d). For all links $j < i$, the length is the distance between the two joints $\|\mathbf{p}_{j-1,j}\|_2 = l_j = \|\mathbf{p}_{j,2}^r - \mathbf{p}_{j,1}^r\|_2$, and for the i -th link, the length is the maximal distance a point can have from the i -th joint $\|\mathbf{r}_{i-1,i}\|_2 \leq l_i = \|\mathbf{p}_{i,2}^r - \mathbf{p}_{i,1}^r\|_2 + r_i^r$. \square

APPENDIX B

SAFETY OF COMBINED BODY PARTS

This section proves that verifying against the constraint for combined body parts guarantees safety.

Proposition B.1. *Verifying against the constraint in (40) with the properties in (39a) – (39c) guarantees the safety of multiple body parts against clamping.*

Proof. We show that (a) all possible contacts between the robot and any combined body part are detected, (b) potential constrained contacts are always detected, and (c) the contact energy is below the thresholds for all body parts in the

combined body part. Let $h_{\tilde{j}}$ be the combined body part constructed from the elements of $\mathcal{H}_{c,a} \in \mathcal{H}_c$.

Proving (a) If and only if the reachable occupancy of a robot link intersects any reachable occupancy of any body in the combined body part, it intersects with the reachable occupancy of the combined body

$$\begin{aligned} \exists h_{j'} \in \mathcal{H}_{c,a} : \mathcal{O}_{j'}^h([t_a, t_b]) \cap \mathcal{O}_i^r([t_a, t_b]) &\neq \emptyset \\ \iff \mathcal{O}_{\tilde{j}}^h([t_a, t_b]) \cap \mathcal{O}_i^r([t_a, t_b]) &\neq \emptyset, \end{aligned} \quad (73)$$

due to the relation in (39b), which directly proves (a).

Proving (b) We first show that all possible ECCs and SCCs are detected. If we replace $\mathcal{O}_i^r([t_a, t_b])$ in (73) with \mathcal{O}_k^e for ECCs we directly show the validity of $\bar{c}_{\{\text{type}\}, i, \tilde{j}, k}([t_a, t_b])$. The same applies for ECCs, where we replace $\mathcal{O}_i^r([t_a, t_b])$ in (73) with $\mathcal{O}_i^r([t_a, t_b])$. Since a set of human bodies can only be clamped if they touch, verifying the constraints in (16) and (17) against the diameter in (39a) trivially ensures safety. The robot velocity constraint in (31) and the robot topology constraint in (34) are independent of the human body part, so safety remains guaranteed. Therefore, the extended constraints for reducing conservatism in (35) and (36) still hold.

Proving (c) As $T_i < \min(T_{i,j}, T_{i,j'}) \iff T_i < T_{i,j} \wedge T_i < T_{i,j'}$, the contact energy threshold in (39c) ensures that no contact energy threshold of any body part in $\mathcal{H}_{c,a}$ is violated if $c_{T, \text{clamp}, i, \tilde{j}}$ is not violated. \square

ACKNOWLEDGMENT

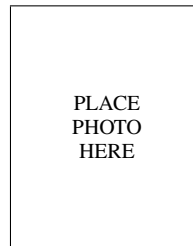
The authors gratefully acknowledge financial support by the Horizon 2020 EU Framework Project CONCERT under grant 101016007 and financial support by the DAAD program Konrad Zuse Schools of Excellence in Artificial Intelligence, sponsored by the Federal Ministry of Education and Research.

REFERENCES

- [1] J. Trevelyan, W. R. Hamel, and S.-C. Kang, "Robotics in hazardous applications," in *Springer Handbook of Robotics*. Springer International Publishing, 2016, pp. 1521–1548.
- [2] J. Smids, S. Nyholm, and H. Berkers, "Robots in the workplace: A threat to—or opportunity for—meaningful work?" *Philosophy & Technology*, vol. 33, no. 3, pp. 503–522, 2020.
- [3] I. Research, "Size of the market for industrial robots worldwide from 2018 to 2020, with a forecast through 2028 (in billion u.s. Dollars)." Statista, Tech. Rep., 2021.
- [4] Statista, "Industry 4.0: In-depth market analysis," Tech. Rep., 2023.
- [5] K. Suita, Y. Yamada, N. Tsuchida, K. Imai, H. Ikeda, and N. Sugimoto, "A failure-to-safety "kyozon" system with simple contact detection and stop capabilities for safe human-autonomous robot coexistence," in *Proc. of the IEEE Int. Conf. on Robotics and Automation (ICRA)*, vol. 3, 1995, pp. 3089–3096.
- [6] K. Kokkalis, G. Michalos, P. Aivaliotis, and S. Makris, "An approach for implementing power and force limiting in sensorless industrial robots," *Procedia CIRP*, vol. 76, pp. 138–143, 2018.
- [7] P. Svarny, M. Tesar, J. K. Behrens, and M. Hoffmann, "Safe physical HRI: Toward a unified treatment of speed and separation monitoring together with power and force limiting," in *Proc. of the IEEE/RSJ Int. Conf. on Intelligent Robots and Systems (IROS)*, 2019, pp. 7580–7587.
- [8] N. Lucci, B. Lacevic, A. M. Zanchettin, and P. Rocco, "Combining speed and separation monitoring with power and force limiting for safe collaborative robotics applications," *IEEE Robotics and Automation Letters*, vol. 5, no. 4, pp. 6121–6128, 2020.
- [9] S. Ergun, Y. Ding, H. Alagi, C. Schöffmann, B. Ubezio, G. Soti, M. Rathmair, S. Mühlbacher-Karrer, U. Thomas, B. Hein, M. Hofbauer, and H. Zangl, "A unified perception benchmark for capacitive proximity sensing towards safe human-robot collaboration (HRC)," in *Proc. of the IEEE Int. Conf. on Robotics and Automation (ICRA)*, 2021, pp. 3634–3640.
- [10] T. Steinecker, A. Kurdas, N. Mansfeld, M. Hamad, R. J. Kirschner, S. Abdolshah, and S. Haddadin, "Mean reflected mass: A physically interpretable metric for safety assessment and posture optimization in human-robot interaction," in *Proc. of the IEEE Int. Conf. on Robotics and Automation (ICRA)*, 2022, pp. 11 209–11 215.
- [11] S. Haddadin, S. Haddadin, A. Khoury, T. Rokahr, S. Parusel, R. Burgkart, A. Bicchi, and A. Albu-Schäffer, "On making robots understand safety: Embedding injury knowledge into control," *The International Journal of Robotics Research*, vol. 31, no. 13, pp. 1578–1602, 2012.
- [12] D. Beckert, A. Pereira, and M. Althoff, "Online verification of multiple safety criteria for a robot trajectory," in *Proc. of the IEEE Conf. on Decision and Control (CDC)*, 2017, pp. 6454–6461.
- [13] S. B. Liu and M. Althoff, "Online verification of impact-force-limiting control for physical human-robot interaction," in *Proc. of the IEEE/RSJ Int. Conf. on Intelligent Robots and Systems (IROS)*, 2021, pp. 777–783.
- [14] J. Lachner, F. Allmendinger, E. Hobert, N. Hogan, and S. Stramigioli, "Energy budgets for coordinate invariant robot control in physical human–robot interaction," *The International Journal of Robotics Research*, vol. 40, no. 8-9, pp. 968–985, 2021.
- [15] R. J. Kirschner, N. Mansfeld, S. Abdolshah, and S. Haddadin, "Experimental analysis of impact forces in constrained collisions according to ISO/ts 15066," in *IEEE Int. Conf. on Intelligence and Safety for Robotics (ISR)*, 2021, pp. 1–5.
- [16] R. J. Kirschner, J. Yang, E. Elshani, C. M. Micheler, T. Leibbrand, D. Müller, C. Glowalla, N. Rajaei, R. Burgkart, and S. Haddadin, "Towards unconstrained collision injury protection data sets: Initial surrogate experiments for the human hand," in *Proc. of the IEEE/RSJ Int. Conf. on Intelligent Robots and Systems (IROS)*, 2024, pp. 14 012–14 019.
- [17] ISO, "Robotics - safety requirements - part 2: Industrial robot applications and robot cells," International Organization for Standardization, Tech. Rep. ISO/FDIS 10218-2:2024-04, 2024.

- [18] J. Vorndamme, A. Melone, R. Kirschner, L. Figueredo, and S. Haddadin, "Safe robot reflexes: A taxonomy-based decision and modulation framework," *IEEE Transactions on Robotics*, vol. 41, pp. 982–1001, 2025.
- [19] J. Thumm and M. Althoff, "Provably safe deep reinforcement learning for robotic manipulation in human environments," in *Proc. of the IEEE Int. Conf. on Robotics and Automation (ICRA)*, 2022, pp. 6344–6350.
- [20] J. A. Marvel and R. Norcross, "Implementing speed and separation monitoring in collaborative robot workcells," *Robotics and computer-integrated manufacturing*, vol. 44, pp. 144–155, 2017.
- [21] B. Lacevic, A. M. Zanchettin, and P. Rocco, "Towards the exact solution for speed and separation monitoring for improved human-robot collaboration," in *Proc. of the IEEE Int. Symp. on Robot and Human Interactive Communication (ROMAN)*, 2020, pp. 1190–1195.
- [22] A. Pereira and M. Althoff, "Overapproximative human arm occupancy prediction for collision avoidance," *IEEE Transactions on Automation Science and Engineering*, vol. 15, no. 2, pp. 818–831, 2018.
- [23] M. Althoff, A. Giusti, S. B. Liu, and A. Pereira, "Effortless creation of safe robots from modules through self-programming and self-verification," *Science Robotics*, vol. 4, no. 31, pp. 1–14, 2019.
- [24] S. Schepp, J. Thumm, S. B. Liu, and M. Althoff, "SaRA: A tool for safe human-robot coexistence and collaboration through reachability analysis," in *Proc. of the IEEE Int. Conf. on Robotics and Automation (ICRA)*, 2022, pp. 4312–4317.
- [25] S. Haddadin, A. Albu-Schäffer, and G. Hirzinger, "Requirements for safe robots: Measurements, analysis and new insights," *The International Journal of Robotics Research*, vol. 28, no. 11-12, pp. 1507–1527, 2009.
- [26] R. J. Kirschner, N. Mansfeld, G. G. Peña, S. Abdolshah, and S. Haddadin, "Notion on the correct use of the robot effective mass in the safety context and comments on ISO/ts 15066," in *IEEE Int. Conf. on Intelligence and Safety for Robotics (ISR)*, 2021, pp. 6–9.
- [27] O. Khatib, "Inertial properties in robotic manipulation: An object-level framework," *The International Journal of Robotics Research*, vol. 14, no. 1, pp. 19–36, 1995.
- [28] F. Benzi, F. Ferraguti, and C. Secchi, "Energy tank-based control framework for satisfying the ISO/ts 15066 constraint," *IFAC-PapersOnLine*, vol. 56, no. 2, pp. 1288–1293, 2023.
- [29] C. Sloth and H. G. Petersen, "Computation of safe path velocity for collaborative robots," in *Proc. of the IEEE/RSJ Int. Conf. on Intelligent Robots and Systems (IROS)*, 2018, pp. 6142–6148.
- [30] P. Aivaliotis, S. Aivaliotis, C. Gkourmelos, K. Kokkalis, G. Michalos, and S. Makris, "Power and force limiting on industrial robots for human-robot collaboration," *Robotics and Computer-Integrated Manufacturing*, vol. 59, pp. 346–360, 2019.
- [31] A. Golshani, A. Kouhkord, A. Ghanbarzadeh, and E. Najafi, "Control design for safe human-robot collaboration based on ISO/ts 15066 with power and force limit," in *Proc. of the Int. Conf. on Robotics and Mechatronics (ICRoM)*, 2023, pp. 279–284.
- [32] M. Hamad, A. Kurdas, N. Mansfeld, S. Abdolshah, and S. Haddadin, "Modularize-and-conquer: A generalized impact dynamics and safe precollision control framework for floating-base tree-like robots," *IEEE Transactions on Robotics*, pp. 1–22, 2023.
- [33] A. Pupa, M. Minelli, and C. Secchi, "A time-optimal energy planner for safe human-robot collaboration," in *Proc. of the IEEE Int. Conf. on Robotics and Automation (ICRA)*, 2024, pp. 17 373–17 379.
- [34] W. Eisenmenger, "Spitze, scharfe und halbscharfe gewalt," in *Handbuch Gerichtliche Medizin*. Springer Berlin, 2004, vol. 1, pp. 571–592.
- [35] B. Povse, D. Koritnik, T. Bajd, and M. Munih, "Correlation between impact-energy density and pain intensity during robot-man collision," in *Proc. of the IEEE RAS & EMBS Int. Conf. on Biomedical Robotics and Biomechanics (BIOROB)*, 2010, pp. 179–183.
- [36] R. Behrens and N. Elkmann, "Study on meaningful and verified thresholds for minimizing the consequences of human-robot collisions," in *Proc. of the IEEE Int. Conf. on Robotics and Automation (ICRA)*, 2014, pp. 3378–3383.
- [37] R. Behrens, G. Pliske, S. Piatek, F. Walcher, and N. Elkmann, "A statistical model to predict the occurrence of blunt impact injuries on the human hand-arm system," *Journal of Biomechanics*, vol. 151, 2023.
- [38] Y. Yamada, Y. Hirasawa, S. Huang, and Y. Umetani, "Fail-safe human/robot contact in the safety space," in *Proc. of the IEEE Int. Workshop on Robot and Human Communication (RO-MAN)*, 1996, pp. 59–64.
- [39] U. Asad, S. Rasheed, W. A. Lughmani, T. Kazim, A. Khalid, and J. Pannek, "Biomechanical modeling of human-robot accident scenarios: A computational assessment for heavy-payload-capacity robots," *Applied Sciences*, vol. 13, no. 3, 2023.
- [40] R. J. Kirschner, C. M. Micheler, Y. Zhou, S. Siegner, M. Hamad, C. Glowalla, J. Neumann, N. Rajaei, R. Burgkart, and S. Haddadin, "Towards safe robot use with edged or pointed objects: A surrogate study assembling a human hand injury protection database," in *Proc. of the IEEE Int. Conf. on Robotics and Automation (ICRA)*, 2024.
- [41] T. Gan, M. Chen, Y. Li, B. Xia, and N. Zhan, "Reachability analysis for solvable dynamical systems," *IEEE Transactions on Automatic Control*, vol. 63, no. 7, pp. 2003–2018, 2018.
- [42] M. Althoff, "An introduction to CORA 2015," in *EPiC Series in Computing*, vol. 34, 2015, pp. 120–151.
- [43] ISO, "Safety of machinery - positioning of safeguards with respect to the approach speeds of parts of the human body," International Organization for Standardization, Tech. Rep. DIN EN ISO 13855:2010-10 ST N, 2010.
- [44] S. Kumar, S. Arora, and F. Sahin, "Speed and separation monitoring using on-robot time-of-flight laser-ranging sensor arrays," in *IEEE Int. Conf. on Automation Science and Engineering (CASE)*, 2019, pp. 1684–1691.

- [45] U. B. Himmelsbach, T. M. Wendt, and M. Lai, "Towards safe speed and separation monitoring in human-robot collaboration with 3D-time-of-flight cameras," in *Proc. of the IEEE Int. Conf. on Robotic Computing (IRC)*, 2018, pp. 197–200.
- [46] M. J. Rosenstrauch, T. J. Pannen, and J. Krüger, "Human robot collaboration - using kinect V2 for ISO/ts 15066 speed and separation monitoring," *Procedia CIRP*, vol. 76, pp. 183–186, 2018.
- [47] B. Yang, S. Xie, G. Chen, Z. Ding, and Z. Wang, "Dynamic speed and separation monitoring based on scene semantic information," *Journal of Intelligent & Robotic Systems*, vol. 106, no. 2, 2022.
- [48] S. Fujii and Q.-C. Pham, "Real-time batched distance computation for time-optimal safe path tracking," in *Proc. of the IEEE Int. Conf. on Robotics and Automation (ICRA)*, 2024, pp. 13 383–13 389.
- [49] S. B. Liu, B. Schürmann, and M. Althoff, "Guarantees for real robotic systems: Unifying formal controller synthesis and reachset-conformant identification," *IEEE Transactions on Robotics*, vol. 39, no. 5, pp. 3776–3790, 2023.
- [50] S. B. Liu and M. Althoff, "Reachset conformance of forward dynamic models for the formal analysis of robots," in *Proc. of the IEEE/RSJ Int. Conf. on Intelligent Robots and Systems (IROS)*, 2018, pp. 370–376.
- [51] S. Bi, C. Yuan, C. Liu, J. Cheng, W. Wang, and Y. Cai, "A survey of low-cost 3D laser scanning technology," *Applied Sciences*, vol. 11, no. 9, 2021.
- [52] P. Schneider and D. H. Eberly, *Geometric Tools for Computer Graphics*. Morgan Kaufmann Publishers, 2003.
- [53] S. Boyd and L. Vandenberghe, *Convex Optimization*, 7th ed. Cambridge University Press, 2009.
- [54] B. Siciliano, L. Sciavicco, L. Villani, and G. Oriolo, *Robotics: Modelling, Planning and Control*. Springer, 2009.
- [55] J. Hopcroft and R. Tarjan, "Algorithm 447: Efficient algorithms for graph manipulation," *Commun. ACM*, vol. 16, no. 6, pp. 372–378, 1973.
- [56] ISO, "Robotics - safety requirements - part 1: Industrial robots," International Organization for Standardization, Tech. Rep. DIN EN ISO 10218-1:2021-09 DC, 2021.
- [57] S. S. Shapiro and M. B. Wilk, "An analysis of variance test for normality (complete samples)," *Biometrika*, vol. 52, no. 3 and 4, pp. 591–611, 1965.
- [58] F. Wilcoxon, "Individual comparisons by ranking methods," *Biometrics Bulletin*, vol. 1, no. 6, pp. 80–83, 1945.
- [59] ISO, "Robots and robotic devices - collaborative robots," International Organization for Standardization, Tech. Rep. ISO/TS 15066:2016(E), 2016.
- [60] A. De Luca, A. Albu-Schaffer, S. Haddadin, and G. Hirzinger, "Collision detection and safe reaction with the dlr-iii lightweight manipulator arm," in *Proc. of the IEEE/RSJ Int. Conf. on Intelligent Robots and Systems (IROS)*, 2006, pp. 1623–1630.



Jakob Thumm Biography text here.

Leonardo Maglanoc Biography text here.

Julian Balletshofer Biography text here.

Matthias Althoff Biography text here.